

# ISLA: A U-Net for MRI-based acute ischemic stroke lesion segmentation with deep supervision, attention, domain adaptation, and ensemble learning

Vincent Roca<sup>a,\*</sup>, Martin Bretzner<sup>a,b,c</sup>, Hilde Henon<sup>d</sup>, Laurent Puy<sup>b,d</sup>, Grégory Kuchcinski<sup>a,b,c</sup>, Renaud Lopes<sup>a,b,e</sup>

<sup>a</sup>Univ. Lille, CNRS, Inserm, CHU Lille, Institut Pasteur de Lille, US 41 - UAR 2014 - PLBS, F-59000 Lille, France

<sup>b</sup>Univ. Lille, Inserm, CHU Lille, U1172 - Lille Neurosciences & Cognition, F-59037 Lille, France

<sup>c</sup>CHU Lille, Département de Neuroradiologie, F-59037 Lille, France

<sup>d</sup>CHU Lille, Département de Neurologie vasculaire, F-59037 Lille, France

<sup>e</sup>CHU Lille, Département de Médecine Nucléaire, F-59037 Lille, France

## Abstract

Accurate delineation of acute ischemic stroke lesions in MRI is a key component of stroke diagnosis and management. In recent years, deep learning models have been successfully applied to the automatic segmentation of such lesions. While most proposed architectures are based on the U-Net framework, they primarily differ in their choice of loss functions and in the use of deep supervision, residual connections, and attention mechanisms. Moreover, many implementations are not publicly available, and the optimal configuration for acute ischemic stroke (AIS) lesion segmentation remains unclear. In this work, we introduce ISLA (Ischemic Stroke Lesion Analyzer), a new deep learning model for AIS lesion segmentation from diffusion MRI, trained on three multicenter databases totaling more than 1500 AIS participants. Through systematic optimization of the loss function, convolutional architecture, deep supervision, and attention mechanisms, we developed a robust segmentation framework. We further investigated unsupervised domain adaptation to improve generalization to an external clinical dataset. ISLA outperformed two state-of-the-art approaches for AIS lesion segmentation on an external test set. Codes and trained models will be made publicly available to facilitate reuse and reproducibility.

## 1. Introduction

Stroke is a major cause of mortality and long-term disability, with ischemic strokes accounting for approximately 87% of all cases (Capirossi et al., 2023). Accurate delineation of ischemic lesions in acute MRI is critical for clinical decision-making (Cimflova et al., 2021). Although manual delineation by experts remains the gold standard, it is time-consuming and labor-intensive.

Automatic segmentation of acute ischemic stroke (AIS) lesions has therefore become an active area of research. Supported by the availability of expert-annotated, multicenter MRI datasets such as ISLES 2022 (Hernandez Petzsche et al., 2022), deep learning (DL) has emerged as a powerful tool for AIS lesion segmentation (Abbasi et al., 2023; Luo et al., 2024).

Among proposed methods, U-Net variants dominate the field (Abbasi et al., 2023; Baaklini and Valdés Hernández, 2025; Luo et al., 2024), with design variations including loss functions, deep supervision (DS), residual connections, and attention mechanisms (Baaklini and Valdés Hernández, 2025). However, comparing approaches remains challenging, as most implementations are not publicly accessible (Liu et al., 2021). More broadly, limited reproducibility and reusability represent major obstacles in applying DL in medical imaging (Plis et al., 2024; Roca et al., 2025).

Another persistent limitation in the field is the scarce evaluation of trained models on external test datasets (Baaklini and Valdés Hernández, 2025; Bojsen et al., 2024). Because scanner types, acquisition settings, and operational procedures vary across centers, ensuring model generalizability remains a major challenge (Luo et al., 2024; Zafari-Ghadim et al., 2024). Domain adaptation has therefore emerged as a promising strategy to enhance cross-site robustness of DL models in AIS lesion segmentation (Abbasi et al., 2023; Luo et al., 2024).

Beyond domain adaptation, ensemble learning is another strategy for improving generalization. By combining multiple independently trained models, ensemble approaches can reduce the risk of overfitting, and has already shown benefits in diverse MRI-based segmentation tasks (de la Rosa et al., 2025; Li et al., 2022; Wiltgen et al., 2024).

In this study, we propose ISLA (Ischemic Stroke Lesion Analyzer), a new DL model for AIS lesion segmentation from diffusion MRI. The first ISLA variant corresponds to the best-performing U-Net-based model selected through internal validation, comparing different loss functions, the use of DS, residual versus standard convolutional blocks, and attention mechanisms. We further developed two additional variants: one incorporating domain adaptation via the Mean Teacher (MT) framework, and another employing ensemble learning across multiple base models. Comparative evaluation against two state-of-the-art (SOTA)

\*Corresponding author at: Lille, 59037 France. E-mail address: vincentroca9@outlook.fr

methods on an external test set demonstrated superior performance of ISLA, particularly for the ensemble variant. The code and trained model weights will be made publicly available on GitHub.

## 2. Related works

### 2.1. Loss functions

A common challenge in medical image segmentation is the strong imbalance between foreground and background voxels. For MRI-based AIS lesion segmentation, Clérigues et al. (2019) recommended combining Generalized dice loss (GDL) with binary cross-entropy (BCE), leveraging the class-balancing properties of GDL together with the stable convergence of BCE. Consistent with this recommendation, Abramova et al. (2021) applied this composite loss to hemorrhagic stroke lesion segmentation in computed tomography and reported significantly higher Dice coefficients compared to focal loss, a BCE variant designed to address class imbalance (Lin et al., 2020).

More recently, Yeung et al. (2022) introduced Unified Focal loss (UFL), a generalization of cross-entropy-based and Dice-based loss functions. In comparisons against six widely used losses across five medical image segmentation tasks—including MRI-based brain tumor segmentation—UFL consistently achieved higher Dice coefficients.

### 2.2. Deep supervision

DS introduces loss terms to intermediate outputs, encouraging hidden layers in DL architectures to become more discriminative (Lee et al., 2015). DS has been successfully applied to MRI-based stroke segmentation (Liu et al., 2021; Maqsood et al., 2025; Sheng et al., 2022). Notably, Gómez et al. (2023) reported improved performance for AIS lesion segmentation using DS.

### 2.3. Residual connections

By adding the input directly to the output within convolutional blocks (He et al., 2016), residual connections allow gradients to bypass convolutions, helping to mitigate vanishing gradients. U-Net architectures remain the most widely used for AIS lesion segmentation (Abbasi et al., 2023; Baaklini and Valdés Hernández, 2025; Luo et al., 2024), and many implementations enhance U-Net blocks with residual connections (Alis et al., 2021; Clérigues et al., 2020; Gheibi et al., 2023; Liu et al., 2020).

### 2.4. Attention mechanisms

Attention mechanisms encourage convolutional neural networks to focus on the most informative features. They are commonly categorized into three types: (i) spatial attention, which highlights specific image regions (Schlemper et al., 2019); (ii) channel attention, which emphasizes informative feature channels (Hu et al., 2020); and (iii) hybrid attention, which combines both strategies (Woo et al., 2018). Attention has been widely explored for stroke lesion

segmentation, including spatial attention (Liu et al., 2020; Yu et al., 2020, 2021; Nazari-Farsani et al., 2023; Gómez et al., 2023), channel attention (Abramova et al., 2021), and hybrid attention (Liu et al., 2021; Rahman et al., 2025; Alshehri and Muhammad, 2023).

### 2.5. Ensemble learning

Ensemble methods aggregate multiple models to reduce overfitting and improve prediction stability. In MRI-based segmentation, previous studies have averaged the probability outputs of different U-Net models to obtain more accurate predictions (Li et al., 2022; Wiltgen et al., 2024). To increase diversity among the models, variations in U-Net architectures were introduced. More recently, de la Rosa et al. (2025) improved the performance of three ischemic stroke segmentation models by using majority voting.

### 2.6. Domain adaptation

Systematic differences in MRI data arising from scanner hardware, imaging parameters, and acquisition protocols have long been documented (Abbasi et al., 2024). To mitigate performance drops on external test sets, domain generalization methods aim to improve model robustness across unseen domains (Dinsdale et al., 2021; Yu et al., 2023). However, these approaches usually require training on multiple diverse source domains with balanced label distributions (Dinsdale et al., 2021; Roca et al., 2025) and are not designed to exploit unlabeled target-domain data.

In contrast, domain adaptation leverages target-domain data to improve robustness. Prior studies in AIS lesion segmentation have shown that supervised domain adaptation (SDA) can improve generalization (Alis et al., 2021; Ryu et al., 2025), but these methods require labeled data from the target domain. Unsupervised domain adaptation (UDA), by comparison, uses unlabeled target data to enhance performance (Wang et al., 2022). In the context of MRI-based segmentation of spinal cord grey matter, Perone et al. (2019) adapted the MT approach for UDA and demonstrated improved segmentation accuracy on the target-center test set.

## 3. Materials and methods

### 3.1. Data

This study includes data from two public databases—SOOP (Absher et al., 2024) and ISLES 2022 (Hernandez Petzsche et al., 2022)—as well as a multicenter private database of MR images acquired in routine clinical practice from the Hauts-de-France region (HDF dataset).

The HDF dataset comes from a study that was classified as observational on March 9, 2010 by the *Comité de protection des personnes Nord-Ouest IV*, and the committee protecting personal information of the patient approved the study by December 21, 2010 (n° 10.677). The Data Protection Officer department of the Lille University Hospital attests to the declaration of the implementation

methods of this project, in accordance with the applicable personal data protection regulation, in particular the General Data Protection Regulation (UE) 2016/679.

All participants had ischemic stroke and underwent MRI, including diffusion-weighted imaging (DWI) and T2-weighted fluid-attenuated inversion recovery (FLAIR). Imaging was performed in the acute phase for the SOOP and HDF datasets, and at varying stages from acute to subacute for ISLES. All SOOP and ISLES DWIs were manually annotated for ischemic stroke lesions. The HDF dataset included both annotated and unannotated DWIs for UDA (section 3.2.6).

We used the SOOP and ISLES data for model training. We divided the HDF dataset into two subsets. The first, **HDF-train**, was used to evaluate different model variants, select the best-performing configuration, and retrain the model. The second, **HDF-test**, was reserved for final evaluation and comparison with SOTA approaches. Both HDF-train and HDF-test contained labeled and unlabeled images. The unlabeled images corresponded to different participants scanned at the same centers as the labeled participants and were used exclusively for UDA. HDF-train and HDF-test were fully independent, involving different participants, different acquisition centers (10 in HDF-train and 10 others in HDF-test), and different lesion annotators.

Table 1 summarizes the dataset characteristics. Except for the ISLES dataset, all DWIs had high in-plane resolution (approximately  $1 \times 1 \text{ mm}^2$ ) and large slice thickness (greater than 3 mm). The HDF dataset contained larger lesions than SOOP and ISLES. HDF-test consisted primarily of GE MRI scans, whereas the other datasets were predominantly acquired on Philips systems.

All datasets included stroke in similar regions, with a lower frequency for SOOP and ISLES (Figure 1).

### 3.2. ISLA segmentation

ISLA takes the trace DWI and the corresponding apparent diffusion coefficient map (ADC) as inputs. The full training and inference pipelines are available at GITHUB-LINK.

#### 3.2.1. Preprocessing

To reduce technical variability and facilitate segmentation, three preprocessing steps are applied before feeding the images to the model. First, a brain mask is computed from the DWI with SynthStrip (Hoopes et al., 2022) and then used to skull-strip both the DWI and ADC. Second, the DWI is registered to a reference DWI with FSL-FLIRT (Jenkinson et al., 2002) using six degrees of freedom; the resulting transformation is also applied to the ADC. After registration, the matrix size is  $192 \times 224 \times 32$  voxels (LAS orientation), with an axial pixel size of  $0.9 \text{ mm}^2$  and a slice thickness of 6.0 mm. Finally, brain intensities are normalized with z-score normalization (separately for DWI and ADC) and clipped to the range  $[-5, 5]$ .

#### 3.2.2. Baseline U-Net

To exploit full volumetric information, we implemented a 3D U-Net that takes the entire DWI and ADC volumes as input (Figure 2).

Following Bridge et al. (2022), we did not include re-sampling along the inferior-superior axis, as this dimension was weakly resolved in our images (Section 3.1). To further account for the highest resolution in the left-right and anterior-posterior axes, we set larger kernel sizes in these directions.

We set the same number of convolutional filters as Bridge et al. (2022) at each U-Net level. However, instead of a single convolutional layer per level, we stacked two layers, a common approach in ischemic stroke segmentation (Clérigues et al., 2020; Gheibi et al., 2023; Gómez et al., 2023; Liu et al., 2021; Moon et al., 2022; Nazari-Farsani et al., 2023).

Predicted probabilities are generated using a single  $1 \times 1 \times 1$  convolution followed by a sigmoid activation. At inference, a threshold of 0.5 is applied to derive the final binary prediction (0: no lesion, 1: lesion), and the resulting mask is subsequently mapped back to the original image space using the inverse of the spatial registration applied during preprocessing (Section 3.2.1).

#### 3.2.3. Base models

Based on our literature review (Section 2), we implemented several variants of our baseline U-Net to identify the most effective configurations and to construct an ensemble learning approach (Section 3.2.5). This section details the implemented techniques, and a summary is given in Table 2.

##### 3.2.3.1. Loss functions

We experimented with two loss functions designed to address class imbalance in segmentation tasks: sum of GDL (Sudre et al., 2017) and BCE (GDL-BCE), and UFL (Yeung et al., 2022). For UFL, we adopted the asymmetric variant with the same hyperparameters as Yeung et al. for their 3D segmentation tasks:  $\lambda = 0.5$ ,  $\delta = 0.6$ ,  $\gamma = 0.5$ .

##### 3.2.3.2. Convolutional blocks

We implemented the convolutional blocks of the baseline U-Net architecture (Figure 2) in two configurations: standard sequential convolutional blocks—StdUNet—and residual convolutional blocks—ResUNet.

For StdUNet, we followed the design proposed by Bridge et al. (2022), using Convolution-Normalization-LeakyReLU sequences with a LeakyReLU slope of 0.3, max-pooling in the encoder, and trilinear upsampling in the decoder. Each block contains two *Conv-Norm-LReLU* sequences. To account for the anisotropic resolution of our images, we set the kernel sizes to  $4 \times 4 \times 2$ .

For ResUNet, we drew inspiration from Zhang et al. (2018), incorporating two Normalization-ReLU-Convolution sequences in each convolutional

**Table 1: Characteristics of populations, MRI scanners, diffusion-weighted imaging, and lesions for each dataset.**

dataset	number of participants	field strength, Tesla	manufacturer	axial pixel size, mm <sup>2</sup> <sub>a</sub>	slice thickness, mm <sub>a</sub>	lesion size, ml <sub>b</sub>
SOOP	1266	1.5 (80.1%) 3.0 (19.9%)	Philips (98.3%) GE (1.2%) Siemens (0.5%)	0.95 ± 0.16	6.00 ± 0.04	7.99 ± 32.23
ISLES	250	3.0 (57.6%) unknown (42.4%)	Philips (50.0 %) unknown (48.4%) Siemens (1.6%)	1.88 ± 0.28	2.60 ± 1.15	6.66 ± 19.59
HDF-train	labeled 223	1.5 (95.1 %) 3.0 (4.9 %)	Philips (66.4%) Siemens (32.7%) GE (0.9%)	1.02 ± 0.30	4.77 ± 0.66	16.51 ± 31.88
	unlabeled 627	1.5 (95.1%) 3.0 (4.9%)	Philips (79.6%) Siemens (18.2%) GE (2.2%)	0.97 ± 0.23	4.89 ± 0.61	-
HDF-test	labeled 100 (113) <sup>c</sup>	1.5 (82.3%) 3.0 (17.7%)	GE (70.8 %) Siemens (22.1%) Philips (7.1%)	1.02 ± 0.20	5.54 ± 0.83	12.77 ± 39.05
	unlabeled 633	1.5 (82.3%) 3.0 (17.7%)	GE (71.9%) Siemens (24.6%) Philips (3.5%)	1.00 ± 0.21	5.42 ± 1.04	-

<sup>a</sup>Values are expressed as mean ± standard deviation.

<sup>b</sup>Values are expressed as median ± interquartile range.

<sup>c</sup>The number of manual segmentations is indicated in brackets (13 images segmented by two radiologists).

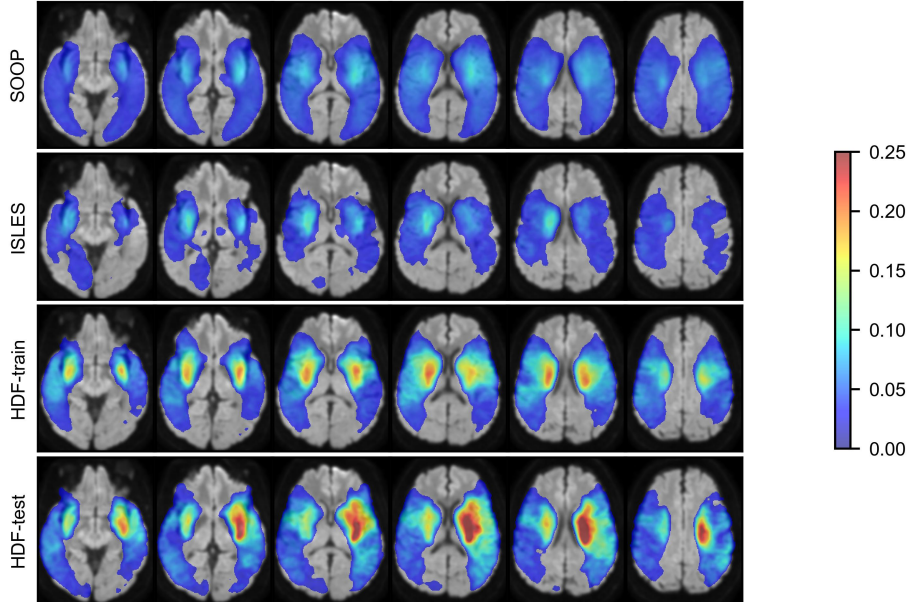


**Figure 1: Proportions of stroke lesions across brain regions and datasets.** The manual lesion delineations were registered in a common space (Section 3.2.1) and the reference trace diffusion-weighted image is shown in background. The proportions masks were smoothed with a gaussian filter (FWHM = 4 mm) and values below 0.02 were masked.

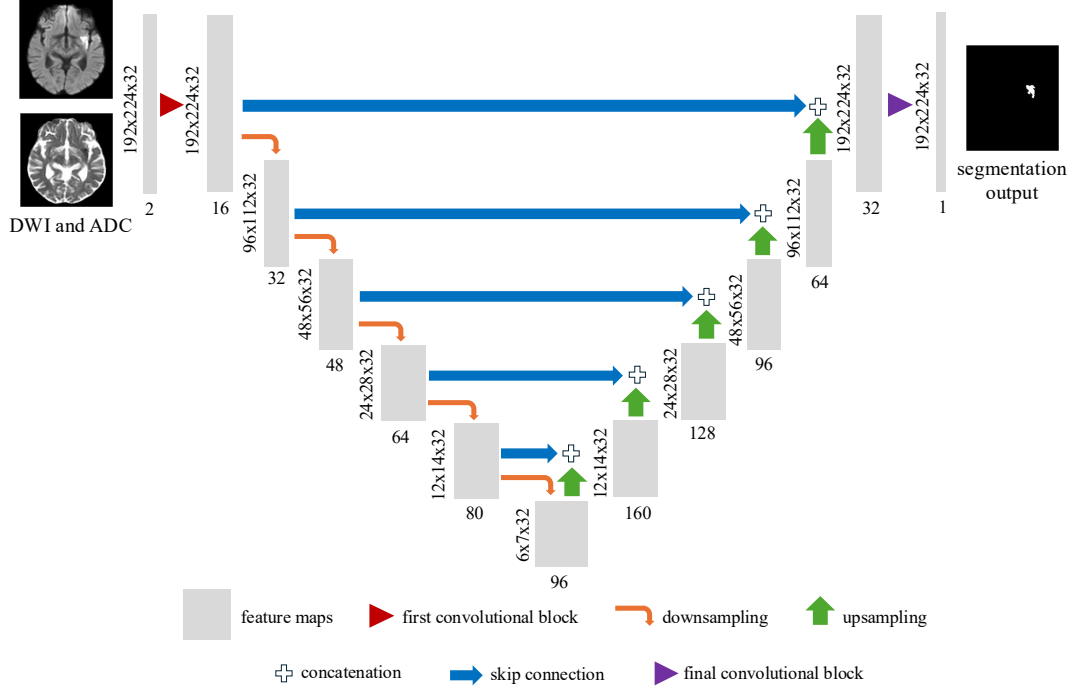


**Figure 2: Architecture of the ISLA baseline.** The number and size of the feature maps are indicated below and to the left of the gray boxes, respectively.

block—except for the first block, which follows a *Conv-Norm-ReLU-Conv* structure. Residual connections are formed by adding each block’s input and output, with identity mappings implemented via  $1 \times 1 \times 1$  convolutions. Downsampling in the encoder is performed using strided convolutions, while trilinear interpolation is used for upsampling in the decoder. Kernel sizes are  $3 \times 3 \times 2$  for stride-1 and  $4 \times 4 \times 2$  for stride-2 convolutions.

Dropout layers with a rate of 0.5 are applied in the bottleneck and the first two decoder blocks—after each *Conv-Norm-LReLU* sequence in StdUNet and before the last convolution of each block in ResUNet.

Since limited cross-domain generalization is a well-known limitation of Batch Normalization (Li et al., 2018), we followed Perone et al. (2019) and replaced it with Group Normalization (GN, Wu and He, 2018) in both StdUNet and ResUNet, using 8 groups per GN layer.

### 3.2.3.3. Deep supervision

We implemented DS following a standard approach: at the bottleneck and each decoder stage, a  $1 \times 1 \times 1$  convolution reduces the number of channels to 1, followed by trilinear upsampling to match the original image dimensions, and a sigmoid activation to compute the probability map (Lv et al., 2022). The overall loss becomes

$$L = \sum_{i=1}^6 \alpha_i L_i$$

where  $L_i$  denotes the loss between the ground truth segmentation and the  $i$ -th network output (bottleneck:  $i = 1$ , final output:  $i = 6$ ). We fixed the weighting coefficients as  $\alpha = (0.03, 0.045, 0.05, 0.125, 0.25, 0.5)$  (Gómez et al., 2023).

### 3.2.3.4. Attention modules

For channel attention, we used the *Squeeze-and-Excitation* (SE) block (Hu et al., 2020). Inspired by the *Enc USE-Net* configuration of Rundo et al. (2019), which demonstrated strong generalization across datasets, we placed an SE block after each encoder block to modulate the skip connections—resulting in five SE blocks in total. Following Rundo et al., we set the reduction ratio to 8.

For spatial attention, we employed the *Attention Gate* (AG) module of Schlemper et al. (2019). We implemented two AG variants: AGs, corresponding to the original spatial attention gate described by Schlemper et al., and AGh, a hybrid attention mechanism that learns attention coefficients for each input channel from the encoder (Appendix A). We integrated them in our U-Net architecture as done by Schlemper et al..

We also experimented with two additional hybrid attention modules. The first is the *Convolutional Block Attention Module* (CBAM, Woo et al., 2018), placed after each U-Net encoder stage following Trebing et al. (2021), except that—unlike Trebing et al.—we did not include CBAM in the bottleneck. CBAM was adapted to process 3D feature maps, notably by using  $7 \times 7 \times 3$  convolutions for the spatial attention module. The second, SE-AGs, combines

our implementations of the SE blocks and AGs modules described above.

### 3.2.4. Training details

Models are trained for 300 epochs with a batch size of 8 using the Adam optimizer (Kingma and Ba, 2014) with a linear learning rate decay from  $5 \times 10^{-4}$  to  $5 \times 10^{-6}$  to ensure convergence. Data-augmentation includes random left-right flipping (50% probability), random translation ( $\pm 10, 12$ , and 2 voxels along the left-right, anterior-posterior, and superior-inferior axes, respectively), random rotation ( $\pm 15^\circ$  around the superior-inferior axis), additive gaussian noise on brain intensities (standard deviation sampled between 0 and 0.15 for each image), and random gamma correction ( $\gamma$  sampled between 0.8 and 1.2 for each image). Mixed precision training (Micikevicius et al., 2017) was adopted.

### 3.2.5. Ensemble learning

Inspired by previous works on MRI-based brain segmentation (Section 2.5), we implemented ensemble predictions using the base models described in Section 3.2.3. It consists in averaging multiple output probability maps to obtain an ensemble prediction, prior to binarization and mapping back to the original image space.

### 3.2.6. Unsupervised domain adaptation

In UDA, the source domain—for which labeled data are available—is distinguished from the target domain, which contains only unlabeled data. To leverage the unlabeled data from the HDF-train and HDF-test datasets (Section 3.1), we incorporated ideas from Perone et al. (2019), who adapted the MT approach for UDA in the context of multicenter MRI-based segmentation.

In the MT framework, the model comprises a student and a teacher, two neural networks sharing a common architecture. The student’s weights are updated with stochastic gradient descent using the following loss function:

$$\mathcal{L} = \mathcal{L}_{sup} + \gamma \mathcal{L}_{cons}$$

where  $\mathcal{L}_{sup}$  is the supervised loss,  $\mathcal{L}_{cons}$  is a consistency loss penalizing the difference between student and teacher predictions for the same inputs, and  $\gamma$  is the consistency weight hyperparameter. The teacher weights are updated using an exponential moving average (EMA):

$$\theta'_t = \alpha \theta'_{t-1} + (1 - \alpha) \theta_t$$

where  $\theta$  and  $\theta'$  denote the student and teacher weights, respectively, and  $\alpha$  is the EMA decay hyperparameter.

In our MT implementation, the consistency loss is computed as the mean squared difference between the student and teacher probability maps. As recommended by French et al. (2017) for UDA, this loss is calculated only on data from the target domain. During a 60-epoch ramp-up phase, the EMA decay is set to 0.99 and then increased to 0.999 for the remainder of training (Tarvainen and

Valpola, 2017). The consistency weight parameter is also gradually increased with a sigmoid ramp-up (Perone et al., 2019) during this ramp-up phase. For data-augmentation on the target-domain images, the same spatial transformations (flipping, translation and rotation) are applied to both student and teacher inputs—to avoid inconsistent prediction maps—whereas different intensity transformations (gaussian noise and gamma correction) are used to further regularize the student’s training. Dropout was removed from the teacher, as it was found to provide only marginal improvements (Tarvainen and Valpola, 2017). At inference, the teacher model is used for prediction. A batch size of 8 was used for both  $\mathcal{L}_{sup}$  and  $\mathcal{L}_{cons}$ .

## 3.3. Experiments

### 3.3.1. Segmentation metrics and method ranking

To quantify the agreement between the predicted and ground truth segmentation masks, we used the same metrics as in the ISLES 2022 challenge (Hernandez Petzsche et al., 2022): Dice similarity coefficient (DSC) and absolute volume difference (AVD, in ml) as voxel-level metrics, and absolute lesion count difference (ALD) and lesion detection F1 score (F1) as lesion-level metrics. In addition, following previous AIS segmentation studies (Clèrigues et al., 2019; Liu et al., 2020; Platscher et al., 2022; Moon et al., 2022; Li et al., 2024), we included the Hausdorff Distance (HD) to account for the distance (in mm) between the predicted and ground truth segmentation masks. Specifically, we computed the 95th percentile of HD (HD95):

$$\begin{aligned} d(a, B) &= \min_{b \in B} \|a - b\|_2 \quad \text{point-to-set distance} \\ HD95(A, B) &= \max \left\{ Q_{0.95} \{d(a, B) : a \in A\} \right. \\ &\quad \left. Q_{0.95} \{d(b, A) : b \in B\} \right\} \end{aligned}$$

Based on these five metrics, we used the case-level ranking procedure of the ISLES 2022 challenge (Hernandez Petzsche et al., 2022) to compare segmentation models applied on the same dataset: (i) computing a metric-specific rank for each case (i.e., segmentation), (ii) calculating the mean rank for each metric, and (iii) averaging these mean ranks to obtain the final ranking.

### 3.3.2. Optimization on internal validation set

In a first set of experiments, we trained models on the SOOP and ISLES datasets and evaluated them on the labeled HDF-train dataset (i.e., the validation set) using the aforementioned metrics to define three ISLA variants: **ISLA-B**, the best-performing base model; **ISLA-MT**, obtained by adapting ISLA-B with our MT framework (Section 3.2.6) using the unlabeled HDF-train dataset for UDA; and **ISLA-ENS**, an optimized set of base models combined using our ensemble strategy (Section 3.2.5).

To identify the best base model without exhaustively evaluating all 48 possible variants (Section 3.2.3), we first

**Table 2: Summary of the base model variants.**

loss function (loss)	GDL-BCE	sum of Generalized dice loss (Sudre et al., 2017) and binary cross-entropy
	UFL	Unified Focal loss (Yeung et al., 2022)
convolutional blocks (block)	StdUNet	<i>Convolution-GN-LeakyReLU</i> sequences
	ResUNet	<i>GN-ReLU-Convolution</i> sequences with residual connections
deep supervision (DS)	✓	loss terms added to intermediate network outputs
	×	no deep supervision
attention mechanisms (att)	SE	squeeze-and-excitation (SE) block (Hu et al., 2020) for skip connection modulation after encoder blocks
	AGs	spatial attention gate module (Schlemper et al., 2019) for fusing encoder and decoder outputs
	AGh	hybrid variant of AGs that learns channel-specific attention coefficients applied to each encoder channel
	CBAM	convolutional block attention module (Woo et al., 2018) for skip connection modulation after encoder blocks
	SE-AGs	SE block for skip connection modulation after encoder blocks and AGs to fuse it with decoder outputs
	×	no attention module

assessed the 8 variants without attention mechanisms. We then evaluated the strongest of these variants with the attention mechanisms and selected ISLA-B using the case-level ranking procedure.

ISLA-MT was obtained by retraining ISLA-B within our MT-based UDA framework and optimizing the consistency-weight hyperparameter on the validation set.

For ISLA-ENS, we explored different model combinations based on the ranking of the base models: *Ensemble 2* (top two models), *Ensemble 3* (top three models), and so on. ISLA-ENS was defined as the ensemble configuration that achieved the best performance on the validation set.

### 3.3.3. Application to external test set

After defining the three ISLA variants, we retrained them on the entire training set—comprising the SOOP, ISLES, and labeled HDF-train datasets—for application to the labeled HDF-test dataset (i.e., the external test set). For ISLA-MT, the unlabeled portion of HDF-test was used for UDA.

#### 3.3.3.1. State-of-the-art comparison approaches

We compared these models against two SOTA DL algorithms: DAGMNet (Liu et al., 2021) and DeepISLES (de la Rosa et al., 2025). We chose these models because they were publicly available online<sup>1</sup> (code and trained model

weights).

DAGMNet infers segmentation masks from DWI and ADC. DeepISLES is an ensemble model combining the three top-performing models from the ISLES 2022 challenge. In addition to DWI and ADC, we included FLAIR images acquired during the same session as DWI for DeepISLES inference as one of its three sub-models requires them.

#### 3.3.3.2. Quantitative evaluations

Segmentation metrics were computed from the output masks of the three ISLA variants and the two SOTA models. We analyzed their distributions on the full test set and within groups stratified by lesion size: small lesions ( $< 5$  ml), medium lesions ( $\geq 5$  and  $< 20$  ml), and large lesions ( $\geq 20$  ml). In addition, we ranked the models using the previously described case-level ranking procedure.

#### 3.3.3.3. Qualitative evaluations

We conducted qualitative comparisons between the best-performing SOTA and ISLA models.

First, within each lesion-size group, we selected for visualization axial slices from the volumes closest to the first, second, and third quartiles of the DSC difference between the two models, excluding cases whose DSC deviated by more than 0.2 from the respective model-specific median within the group.

Second, for both models, we computed four voxel-wise maps over the full test set: the proportions of false positives (FP) and false negatives (FN), as well as the mean

<sup>1</sup>DAGMNet: <https://www.nitrc.org/projects/ads> accessed 2025-01-15; DeepISLES: <https://github.com/ezequieldlrosa/DeepISLES> accessed 2025-07-25

HD (in mm) of FP and FN voxels with respect to the ground truth and predicted masks, respectively. To generate these maps, we retained one manual annotation per patient—removing 13 duplicated readings—and assigned a value of 0 to voxels predicted as negative (for the FP mean HD map) and to voxels predicted as positive (for the FN mean HD map).

All visualizations were produced using MR images registered to a common space (Section 3.2.1). The voxel-wise maps were smoothed with a gaussian filter (FWHM = 4 mm) and thresholded at 1% (for proportions) and 0.2 mm (for distances).

## 4. Results

### 4.1. Optimization on internal validation set

#### 4.1.1. Performance ranking of the base models

After the preliminary evaluation of the base models without attention mechanisms, we excluded the GDL-BCE loss due to its poor performance compared to UFL (Appendix B).

Results for all base models trained with UFL are reported in Table 3. The models trained with DS outperformed those without DS on almost all metrics—except for the ResUNet without attention, which was slightly worse with DS. The benefit of DS was more pronounced when combined with attention mechanisms. Among these, although no single attention module consistently outperformed the others, variants including an AG module tended to be slightly better ranked. A similar observation applies to the type of convolutional block: StdUNet was more often better ranked than ResUNet, though not consistently. The StdUNet variant with DS and SE-AGs was the top-performing base model, and thus defined as ISLA-B.

#### 4.1.2. Mean Teacher

Validation results for MT versions of the best base model are presented in Appendix C. Variants with low consistency weights (1 or 5) were slightly better ranked than the variant without MT, primarily for DSC and HD95. The variant with a consistency weight of 5 achieved the best ranking and was therefore defined as ISLA-MT.

#### 4.1.3. Ensemble learning

Validation results for the ensemble approaches are reported in Table 4. As expected—given that the ensembles share constituent models—the median metric values were relatively similar across approaches. However, all ensemble models were clearly better than the best base model according to the case-level ranking. Approaches combining either few or many models (e.g., *Ensemble 2* and *Ensemble 24*) performed worse than those combining a moderate number of models. The top-performing approach, *Ensemble 6*, was selected as ISLA-ENS.

### 4.2. Application to external test set

After having defined the three ISLA variants (ISLA-B, ISLA-MT and ISLA-ENS) on the internal validation set, we applied them on the generalization test set.

#### 4.2.1. Quantitative evaluation

Figure 3 shows the distributions of the segmentation metrics on the full external test set, as well as after stratification by lesion size. Across the full test set, both SOTA approaches were outperformed by the ISLA models on all metrics when comparing medians. The ISLA models also exhibited smaller interquartile ranges. The same patterns were observed within each lesion-size stratum, with one exception: DAGMNet achieved DSCs on small lesions that were comparable to those of ISLA-MT; however, ISLA-MT remained clearly superior on the other metrics. Overall, DAGMNet outperformed DeepISLES on DSC, AVD and HD95 but was slightly worse on ALD and F1.

Although establishing a clear hierarchy among the three ISLA variants from Figure 3 is not straightforward, ISLA-ENS demonstrated slightly more consistent performance across metrics and lesion-size strata. Furthermore, the case-level ranking of the evaluated models (Table 5) identified ISLA-ENS as the top-performing model on average across all metrics. It also ranked first on every metric except ALD, for which ISLA-MT achieved the highest score. ISLA-MT was close to ISLA-B across all metrics.

Case-level ranking (Table 5) also indicates that both DAGMNet and DeepISLES performed worse than the ISLA models across all metrics in terms of median values and rankings. Except for ALD and F1, DeepISLES was the lowest-performing method.

#### 4.2.2. Qualitative comparison of DAGMNet and ISLA-ENS

##### 4.2.2.1. Illustrative examples

Figure 4 shows representative examples of segmentations from the test set with DAGMNet and ISLA-ENS, the best SOTA and ISLA models according to the test set case-level ranking (Table 5).

In cases 1 and 2 of Figure 4a, both models successfully detected the lesions; however, DAGMNet slightly underestimated the lesion extent in case 1. In case 3, a corticospinal tract anisotropy artifact resulted in FPs for DAGMNet.

Cases 1 and 3 of Figure 4b further illustrate underestimation of lesion extent by DAGMNet, whereas ISLA-ENS produced segmentations closely matching the manual annotations. In case 2, both models generated FPs due to magnetic-susceptibility artifacts near the nasal region.

In Figure 4c, case 1 shows accurate delineation of the lesion by both models, with no FPs induced by the inhomogeneity artifact. Case 2 demonstrates a missed small cerebellar lesion by ISLA-ENS. In case 3, both models correctly localized the lesion, but DAGMNet again produced FPs caused by magnetic-susceptibility artifacts around the nose.



**Table 3: Case-level ranking on the validation set of the base models trained with Unified Focal Loss.**

model configuration			mean rank	DSC	AVD	ALD	F1	HD95
block	DS	att						
StdUNet	✓	SE-AGs	11.37	0.712 (9.53)	3.481 (12.19)	1 (12.41)	0.667 (10.88)	5.408 (11.81)
ResUNet	✓	AGs	11.48	0.701 (10.46)	3.515 (11.55)	1 (12.22)	0.667 (11.42)	5.609 (11.76)
StdUNet	✓	AGh	11.65	0.710 (10.67)	3.689 (11.95)	1 (12.15)	0.667 (11.54)	5.408 (11.94)
StdUNet	✓	SE	11.81	0.713 (11.50)	3.608 (12.54)	1 (11.42)	0.667 (12.15)	5.377 (11.45)
StdUNet	✓	CBAM	11.82	0.705 (11.32)	3.579 (13.10)	1 (11.76)	0.667 (11.94)	5.502 (10.96)
ResUNet	✓	SE-AGs	11.91	0.698 (12.37)	3.281 (11.84)	1 (11.64)	0.667 (11.49)	5.500 (12.20)
StdUNet	✓	AGs	12.05	0.701 (10.91)	3.923 (12.85)	2 (12.51)	0.667 (11.38)	5.612 (12.58)
ResUNet	✓	CBAM	12.06	0.697 (11.69)	3.560 (12.23)	2 (12.72)	0.667 (11.38)	5.502 (12.28)
ResUNet	✓	SE	12.11	0.700 (11.89)	3.217 (11.63)	2 (12.73)	0.667 (12.48)	5.498 (11.82)
StdUNet	✓	×	12.16	0.692 (11.46)	3.802 (13.46)	1 (11.74)	0.667 (12.09)	5.873 (12.03)
ResUNet	✓	AGh	12.28	0.703 (12.30)	3.366 (12.10)	1 (12.76)	0.667 (11.93)	5.680 (12.32)
StdUNet	×	SE-AGs	12.33	0.690 (12.63)	3.345 (11.97)	1 (12.04)	0.667 (12.16)	6.365 (12.87)
ResUNet	×	×	12.39	0.701 (12.15)	3.762 (12.23)	2 (12.67)	0.667 (12.64)	5.596 (12.25)
ResUNet	✓	×	12.56	0.693 (12.95)	3.305 (12.55)	2 (13.06)	0.667 (11.98)	5.500 (12.28)
ResUNet	×	AGh	12.72	0.683 (13.55)	3.092 (11.12)	2 (12.95)	0.615 (14.20)	5.751 (11.80)
StdUNet	×	AGh	12.75	0.681 (13.66)	3.588 (12.08)	2 (12.36)	0.667 (12.18)	6.972 (13.48)
StdUNet	×	×	12.88	0.691 (12.85)	3.556 (13.12)	2 (12.71)	0.667 (13.16)	5.710 (12.59)
StdUNet	×	AGs	12.93	0.678 (12.95)	3.794 (12.69)	2 (13.01)	0.625 (12.84)	6.623 (13.14)
ResUNet	×	SE	13.13	0.681 (13.30)	3.507 (12.36)	2 (12.91)	0.600 (14.22)	5.958 (12.87)
StdUNet	×	SE	13.19	0.695 (13.91)	3.822 (14.18)	2 (12.34)	0.667 (12.38)	5.609 (13.13)
ResUNet	×	AGs	13.51	0.683 (14.06)	3.186 (12.12)	2 (13.62)	0.636 (13.91)	6.722 (13.81)
StdUNet	×	CBAM	13.53	0.668 (14.33)	3.555 (13.57)	2 (12.44)	0.667 (13.29)	7.188 (14.02)
ResUNet	×	CBAM	13.59	0.680 (14.49)	4.153 (13.46)	2 (12.82)	0.615 (13.89)	6.713 (13.30)
ResUNet	×	SE-AGs	13.79	0.672 (15.06)	3.842 (13.10)	2 (13.02)	0.588 (14.45)	6.479 (13.31)

Mean rank, defined as the mean case-level rank, is used to order the models. Metrics are reported as medians, with the corresponding mean ranks in parentheses.

Table 4: Case-level ranking on the validation set of the ensemble models.

model	mean rank	DSC	AVD	ALD	F1	HD95
Ensemble 6	12.03	0.716 (11.97)	3.604 (12.22)	1 (11.92)	0.667 (12.31)	5.080 (11.75)
Ensemble 18	12.09	0.714 (11.89)	3.334 (11.77)	1 (12.33)	0.667 (12.28)	5.143 (12.19)
Ensemble 16	12.11	0.715 (11.83)	3.280 (11.33)	1 (12.64)	0.667 (12.62)	5.092 (12.15)
Ensemble 19	12.17	0.714 (11.97)	3.330 (11.46)	1 (12.65)	0.667 (12.70)	5.092 (12.09)
Ensemble 12	12.23	0.714 (11.99)	3.455 (12.85)	1 (12.50)	0.667 (11.97)	5.082 (11.85)
Ensemble 17	12.27	0.716 (11.84)	3.298 (11.73)	1 (12.73)	0.667 (12.75)	5.092 (12.30)
Ensemble 5	12.29	0.720 (12.28)	3.608 (12.73)	2 (12.08)	0.667 (12.46)	5.080 (11.88)
Ensemble 15	12.29	0.715 (11.87)	3.387 (12.04)	1 (12.96)	0.667 (12.40)	5.092 (12.17)
Ensemble 8	12.31	0.714 (12.18)	3.632 (12.70)	1 (12.21)	0.667 (12.40)	5.082 (12.08)
Ensemble 14	12.33	0.715 (11.71)	3.379 (12.65)	1 (12.63)	0.667 (12.53)	5.082 (12.15)
Ensemble 9	12.33	0.714 (12.38)	3.488 (12.61)	1 (12.47)	0.667 (12.30)	5.219 (11.92)
Ensemble 10	12.41	0.714 (12.46)	3.575 (13.05)	1 (12.24)	0.667 (12.42)	5.163 (11.86)
Ensemble 21	12.41	0.714 (12.58)	3.285 (11.98)	1 (12.46)	0.667 (12.25)	5.143 (12.78)
Ensemble 7	12.41	0.718 (12.55)	4.000 (12.95)	1 (12.01)	0.667 (12.33)	5.125 (12.20)
Ensemble 13	12.48	0.716 (12.12)	3.374 (12.45)	1 (12.59)	0.667 (12.48)	5.143 (12.75)
Ensemble 20	12.53	0.714 (12.62)	3.252 (12.38)	1 (12.33)	0.667 (12.51)	5.080 (12.80)
Ensemble 4	12.55	0.716 (12.85)	3.665 (12.55)	1 (12.58)	0.667 (12.50)	5.080 (12.25)
Ensemble 23	12.58	0.713 (12.77)	3.265 (12.31)	1 (12.55)	0.667 (12.19)	5.080 (13.10)
Ensemble 22	12.59	0.714 (12.35)	3.171 (12.51)	1 (12.76)	0.667 (12.19)	5.092 (13.15)
Ensemble 11	12.60	0.714 (12.66)	3.558 (13.28)	1 (12.54)	0.667 (12.35)	5.159 (12.18)
Ensemble 3	12.68	0.718 (12.67)	3.358 (12.23)	1 (12.44)	0.667 (12.63)	5.192 (13.41)
Ensemble 24	12.86	0.713 (13.24)	3.189 (12.84)	1 (12.79)	0.667 (12.30)	5.239 (13.11)
Ensemble 2	13.38	0.714 (13.29)	3.287 (13.36)	2 (12.89)	0.667 (13.93)	5.389 (13.41)
Ensemble 1	14.07	0.712 (15.92)	3.481 (14.02)	1 (12.71)	0.667 (13.22)	5.408 (14.48)

Mean rank, defined as the mean case-level rank, is used to order the models. Metrics are reported as medians, with the corresponding mean ranks in parentheses.

Ensemble  $n$  corresponds to the ensemble combining the  $n$  best-ranked base models.

Table 5: Case-level ranking on the test set.

model	mean rank	DSC	AVD	ALD	F1	HD95
ISLA-ENS	2.55	0.754 (2.34)	2.979 (2.42)	1 (2.81)	0.667 (2.67)	6.316 (2.52)
ISLA-MT	2.76	0.734 (2.79)	2.769 (2.70)	1 (2.79)	0.667 (2.79)	6.081 (2.72)
ISLA-B	2.77	0.741 (2.78)	2.879 (2.51)	1 (2.82)	0.667 (2.84)	7.082 (2.89)
DAGMNet	3.19	0.724 (2.95)	3.737 (3.22)	2 (3.40)	0.588 (3.41)	11.620 (2.99)
DeepISLES	3.73	0.512 (4.14)	5.933 (4.15)	2 (3.17)	0.667 (3.29)	18.529 (3.89)

Mean rank, defined as the mean case-level rank, is used to order the models. Metrics are reported as medians, with the corresponding mean ranks in parentheses.

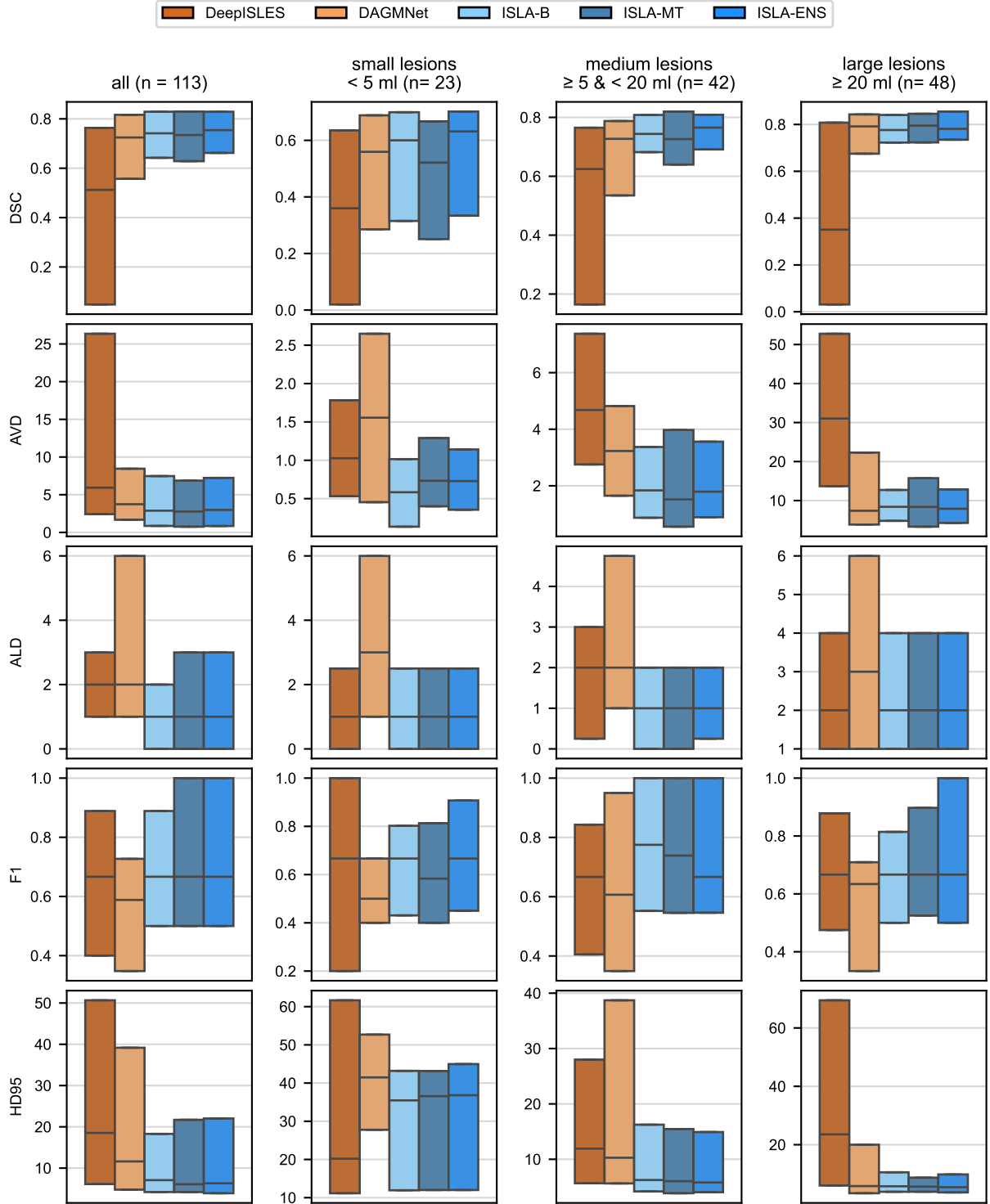


**Figure 3: Segmentation metrics for the test set, reported overall and stratified by lesion size.** Boxplots show median and interquartile range only; whiskers and outliers are omitted for clarity.

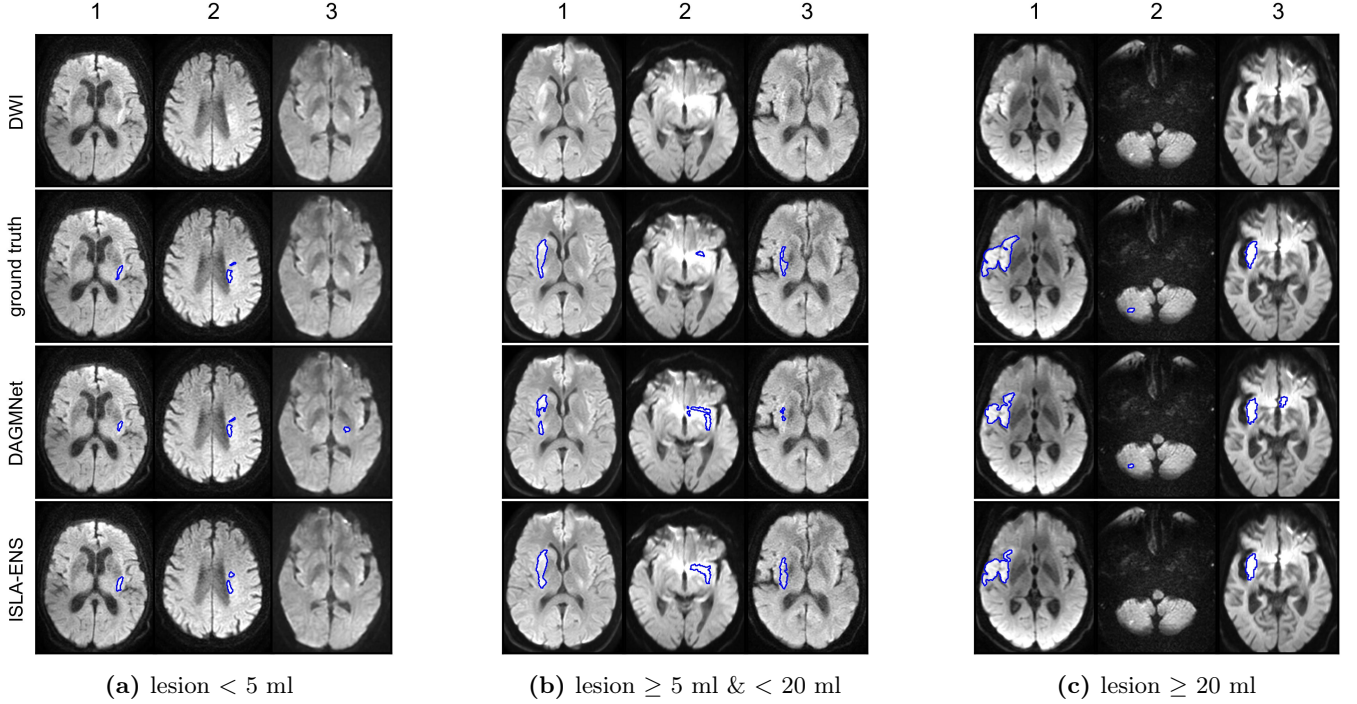


**Figure 4: Illustrative cases of DAGMNet and ISLA-ENS segmentations from the test set.** Axial slices are shown from the volumes closest to the first, second, and third quartiles of the DSC difference between the two models across the test set, excluding cases whose DSC deviated by more than 0.2 from the respective model-specific median within the group. The trace diffusion-weighted image and the segmentation masks were registered in a common space (Section 3.2.1).

#### 4.2.2.2. Proportions and distances of false positives and false negatives

The FP proportion map (Figure 5a) shows that both models exhibited a region of high FP concentration near the right corticospinal tract: slices 5 and 6 for ISLA-ENS, and slices 8 and 9 for DAGMNet. When examining the FN proportion map (Figure 5b) alongside it, it can be seen that the region of high FP concentration for ISLA-ENS coincided with lower FN proportions compared with DAGMNet (slices 5 and 6), whereas the converse was not true (slices 8 and 9). This suggests that ISLA-ENS’s tendency to be more sensitive to suspicious areas contributed to improved lesion detection, a pattern not observed for DAGMNet. In addition, ISLA-ENS produced fewer FPs in the superior posterior region of the brain (slices 5–9 in Figure 5a) and fewer FNs across a large inferior region (slices 1–7 in Figure 5b).

Figure 5c further shows that DAGMNet produced FPs that were, on average, farther from any true lesion compared with ISLA-ENS. For example, slices 5–9 exhibit elevated mean HDs in the posterior part of the brain for DAGMNet; most contributing cases displayed inhomogeneity artifacts (Appendix D). Slices 1–7 also show high mean HDs in the temporal region (particularly the left) for DAGMNet, likely caused by magnetic-susceptibility artifacts near the ears (Appendix D).

To a lesser extent, slices 8 and 9 of Figure 5c reveal two

regions where both models displayed elevated mean HDs: one at the left posterior boundary and another in a small region along the right boundary. These high distances were attributable to a case with a severe inhomogeneity artifact in the former region and a case with a hematoma in the latter (Appendix D).

Regarding FN mean HD, although slightly higher values were observed in the right posterior superior region for ISLA-ENS—corresponding to regions where DAGMNet exhibited substantially higher FP mean HDs (Figure 5c)—, no region showed comparably large average errors (Figure 5d).

## 5. Discussion

Although several DL models for AIS lesion segmentation have been proposed in recent years, few are publicly available, and it remains unclear which architectural components and training strategies are most effective. In this work, we introduced ISLA, an upcoming freely available 3D DL model for MRI-based AIS lesion segmentation, trained on three multicenter databases totaling more than 1500 AIS participants. The model was developed through systematic experiments evaluating loss functions, convolutional architectures, deep supervision, attention mechanisms, domain adaptation, and ensemble learning. Evaluation on an external test set of MR images acquired in rou-

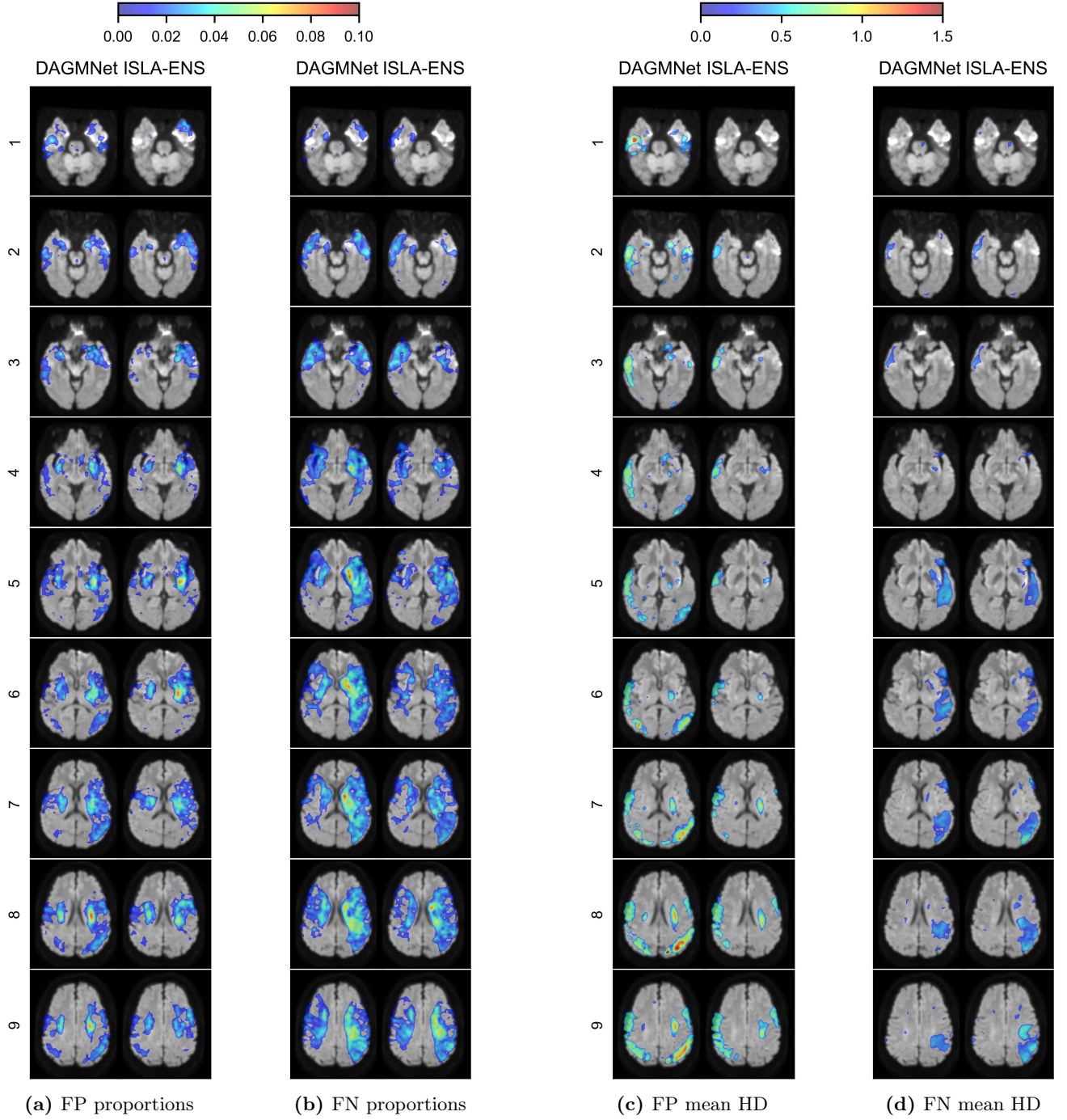


**Figure 5: Voxel-wise maps of false positives (FP) and false negatives (FN) from the test set.** The FP and FN masks were registered into a common space (Section 3.2.1) before computation, and the reference trace diffusion-weighted image is shown in background. The maps were smoothed with a gaussian filter ( $\text{FWHM} = 4 \text{ mm}$ ) and thresholded at 1% (for proportions) and 0.2 mm (for distances). For the Hausdorff distance (HD) maps, one manual annotation was retained per patient, and voxels predicted as negative and positive were assigned a value of 0 in the mean computation of FP and FN, respectively.

tine clinical practice, together with comparisons against two SOTA approaches, demonstrated ISLA’s sensitivity and robustness to MR artifacts across lesion sizes and segmentation metrics.

### 5.1. Comparison of base models on the validation set

In the comparison of loss functions (Section 4.1.1), UFL outperformed GDL-BCE. This aligns with the findings of Yeung et al. (2022), who applied UFL to MRI-based 3D brain tumor segmentation and reported improvements over several commonly used loss functions, including a compound loss similar to GDL-BCE.

The validation results also showed clear performance gains when incorporating DS. Previous works reported that DS, by adding auxiliary supervision at deep layers, helps alleviate the vanishing gradient problem in segmentation networks (Sheng et al., 2022; Lv et al., 2022). Moreover, DS can reduce the risk of overlooking small structures in deep layers (Maqsood et al., 2025), which is particularly relevant for AIS lesion segmentation.

Introducing attention mechanisms further improved segmentation accuracy on the validation set. Similar findings were previously reported in AIS segmentation by Gómez et al. (2023), who combined DS with AG-like blocks, and by Alshehri and Muhammad (2023) using CBAM. Like DS, attention mechanisms are especially suited to the detection of small objects (e.g., AIS lesions), as they guide deep architectures to focus on the most informative regions (Baaklini and Valdés Hernández, 2025; Gómez et al., 2023; Alshehri and Muhammad, 2023). Among the five attention modules evaluated, those incorporating AG modules performed slightly better overall. An example of attention coefficients extracted from the AGs modules of ISLA-B illustrates that the model concentrated attention around the lesion area—especially at higher U-Net resolutions (Appendix E). This observation is consistent with Schlemper et al. (2019), who reported that AG modules combined with DS enhance segmentation performance by reinforcing learning at multiple network scales.

### 5.2. Domain adaptation

The proposed MT strategy for UDA yielded slightly more accurate segmentations on both the validation and test sets (Sections 4.1.2 and 4.2.1). However, given the practical constraints on accessing source labeled data and target unlabeled data, the performance gains may not be sufficient for real-world deployment. In contrast, Perone et al. (2019) achieved substantial improvements in domain generalization using a similar approach for spinal cord gray matter segmentation, and Wang et al. (2023) reported comparable gains using a source-free domain adaptation strategy for ischemic stroke segmentation. A plausible explanation for the discrepancy is the modest size of the source-domain datasets in these studies—60 cases in Perone et al.’s work and fewer than 200 in Wang et al.’s—compared with more than 1500 in our study.

Findings from Ryu et al. (2025) on AIS lesion segmentation further support this hypothesis. Using SDA—which is more restrictive and typically more influential than UDA—the authors observed only slight improvements when the source dataset included 866 or more annotated cases. Moreover, achieving even these small gains required at least 100 manually annotated cases from the target domain. Similarly, Alis et al. (2021) successfully applied SDA for AIS lesion segmentation by leveraging a large number of labeled cases from the target domains (approximately 300).

### 5.3. Ensemble learning

Among the three ISLA variants, the ensemble approach (ISLA-ENS) was clearly the most performant on the test set (Section 4.2.1). Even on the validation set—on which ISLA-B was selected as the top-performing base model, potentially underestimating its prediction errors—all ensemble variants outperformed ISLA-B (Section 4.1.3). These results align with the findings of de la Rosa et al. (2025), who exceeded the performance of the three top-ranked ISLES 2022 models by combining them through a majority-voting scheme.

### 5.4. Comparison with state-of-the-art approaches on the test set

The ISLA variants clearly outperformed DAGMNet and DeepISLES in the quantitative evaluation on the external test set, across all metrics and within all lesion-size strata (Section 4.2.1).

Analysis of the voxel-wise FP mean HD map, together with the representative cases in Appendix D, revealed that DAGMNet produced numerous FPs located far from any true lesion, in contrast to ISLA-ENS. This indicates that ISLA-ENS generated fewer spurious detections unrelated to actual lesions—an essential property for clinical usability. Moreover, the results in Appendix F confirm that DAGMNet primarily underperformed due to lower precision. A plausible explanation is the short interval between stroke onset and MR acquisition in the HDF-test dataset (TODO), as Liu et al. (2021) reported reduced performance of DAGMNet in hyperacute stroke cases.

DeepISLES was nonetheless the lowest-performing model overall, mainly due to low sensitivity (Appendix F). A representative example from the test set illustrates this issue (Appendix G). All three DeepISLES constituent models also showed low segmentation performance on our test set (Appendix H). As with DAGMNet, the short onset-to-scan delay in HDF-test may partly account for this: although de la Rosa et al. (2025) reported that DeepISLES performs robustly across different stroke phases, they also observed its lowest performance in the acute phase compared with the subacute phase and indicated that DeepISLES may be less sensitive in early-acquired MR images.

### 5.5. Limitations and perspectives

The main limitation of our study is the relatively small size of the test set (100 participants). Previous works have evaluated AIS lesion segmentation models on larger databases (Liu et al., 2021; de la Rosa et al., 2025; Ryu et al., 2025; Alis et al., 2021). However, these studies relied on datasets that were private or available only as restricted-use collections under Data Use Agreements, which prevented their inclusion in our work. Despite this, our multicenter test set comprises MR images acquired in emergency stroke services, making it representative of real-world deployment conditions. Furthermore, by publicly releasing our segmentation models, we facilitate future research and enable the ISLA models to be independently evaluated on additional MR datasets.

Another limitation is that we only experimented with U-Net architectures to develop ISLA, despite the increasing number of models integrating Transformers for stroke lesion segmentation (Zafari-Ghadim et al., 2024). We made this choice for two reasons. First, U-Net remains the most widely used architecture in this field (Abbasi et al., 2023; Luo et al., 2024; Baaklini and Valdés Hernández, 2025). Second, when experimenting with UNETR—a U-Net variant that incorporates transformer blocks in the encoder and that has been widely used in medical image segmentation (Hatamizadeh et al., 2022)—we encountered gradient instabilities that prevented the model from converging. Moreover, to capture potential long-range dependencies—the primary motivation for using Transformers—our 3D U-Net processes the full trace DWI and ADC without downsampling, which is uncommon among AIS lesion segmentation models (Baaklini and Valdés Hernández, 2025) and may reduce the need for transformer-based global attention.

## 6. Conclusion

This study introduces ISLA, an upcoming publicly available 3D DL model for AIS lesion segmentation in MRI. ISLA was developed through a systematic exploration of architectural components and training strategies, highlighting the importance of the loss function and the benefits of deep supervision, attention mechanisms, and ensemble learning. Trained on more than 1500 cases from three multicenter datasets, ISLA demonstrated strong and consistent performance on an external clinical test set, outperforming two SOTA approaches across lesion sizes and evaluation metrics. Qualitative analyses further showed high sensitivity to acute stroke lesions and strong robustness to MR artifacts, reducing the occurrence of clinically irrelevant false positives. Future work should extend the validation of ISLA to additional clinical centers and imaging protocols to further assess its generalizability and readiness for real-world deployment.

## Appendix A. Details of the attention gate modules

Figure A.1 illustrates the implementation details of our two attention gate modules.

## Appendix B. Validation results of the base models without attention module

Table B.1 shows the validation-set segmentation metrics for base models trained without attention modules.

## Appendix C. Validation results of the best base model trained with Mean Teacher

Table C.1 shows the validation-set segmentation metrics for MT versions of the best base model with different consistency weights.

## Appendix D. Test set cases with clear false positives from DAGMNet and/or ISLA-ENS

In this section, we provide cases from the test set in which DAGMNet and/or ISLA-ENS produced FPs located far from any true lesion.

Figure D.1 illustrates 7 cases in which DAGMNet generated FPs in the posterior region of the brain, accounting for the large FP HD values observed in that area in the voxel-wise FP mean HD map (Figure 5c). Most of these errors were caused by inhomogeneity artifacts, while others were associated with paramagnetic artifacts. Notably, none of these artifacts induced FPs for ISLA-ENS.

Across the test set, we identified 35 participants (out of 100) for whom DAGMNet produced FPs in the inferior part of the brain (8 for ISLA-ENS). Most of them were caused by magnetic-susceptibility artifacts near the ears (Figure D.2), which also explains the large FP HD values observed in that region in the voxel-wise FP mean HD map (Figure 5c).

Figure D.3 shows a case in which both models were misled by an inhomogeneity artifact, explaining the elevated FP HD values observed in that area in the voxel-wise FP mean HD map (Figure 5c). DAGMNet was more affected than ISLA-ENS in the left posterior inferior region of the brain.

In Figure D.4, the presence of a hematoma caused both models to produce FPs on the right side of the brain, corresponding to the high HDs observed in that area in the voxel-wise FP mean HD map (Figure 5c). Again, DAGMNet was more affected than ISLA-ENS, with the FP lesion extending further superiorly.



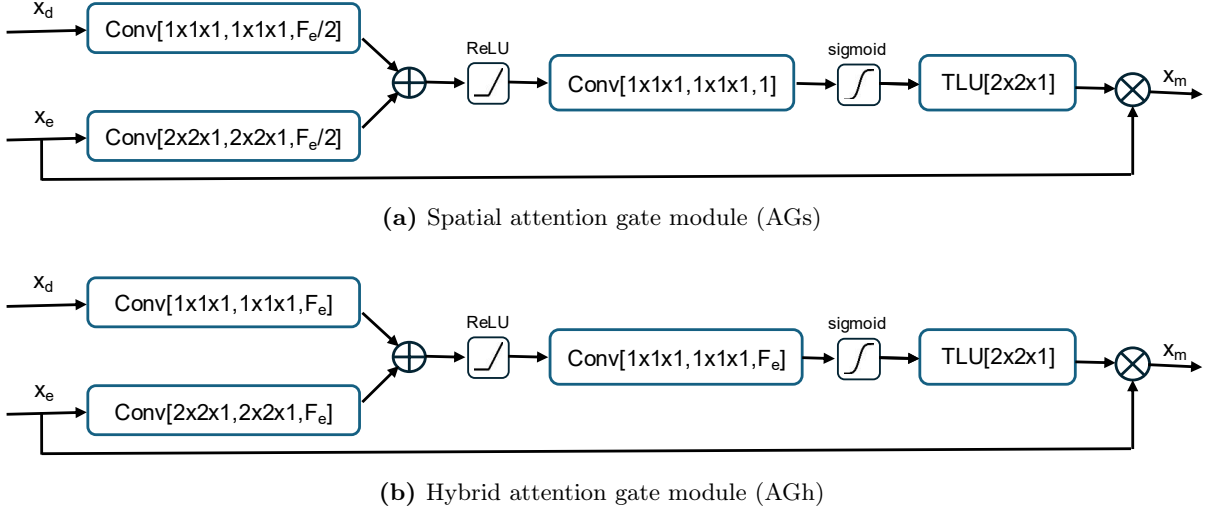


**Figure A.1: Illustration of the implemented attention gate modules.**  $x_d$  denotes the decoder feature maps,  $x_e$  denotes the encoder feature maps, and  $x_m$  the output modulated feature maps.  $\text{Conv}[k_1 \times k_2 \times k_3, s_1 \times s_2 \times s_3, f]$  represents a convolution with  $f$  filters, kernel size  $k_1 \times k_2 \times k_3$ , and stride  $s_1 \times s_2 \times s_3$ .  $\text{TLU}[u_1 \times u_2 \times u_3]$  denotes trilinear upsampling with factors  $u_1 \times u_2 \times u_3$ .

**Table B.1: Case-level ranking on the validation set of the base models trained without attention modules.**

model configuration			mean rank	DSC	AVD	ALD	F1	HD95
block	loss	DS						
StdUNet	UFL	✓	4.17	0.692 (3.70)	3.802 (4.20)	1 (4.26)	0.667 (4.37)	5.873 (4.32)
ResUNet	UFL	×	4.27	0.701 (4.02)	3.762 (3.83)	2 (4.58)	0.667 (4.59)	5.596 (4.35)
ResUNet	UFL	✓	4.30	0.693 (4.22)	3.305 (3.88)	2 (4.67)	0.667 (4.31)	5.500 (4.41)
StdUNet	UFL	×	4.47	0.691 (4.27)	3.556 (4.05)	2 (4.59)	0.667 (4.77)	5.710 (4.64)
ResUNet	GDL-BCE	✓	4.56	0.690 (4.63)	4.151 (4.98)	2 (4.65)	0.667 (4.12)	5.360 (4.43)
StdUNet	GDL-BCE	✓	4.65	0.690 (4.73)	4.626 (5.18)	1 (4.39)	0.667 (4.48)	6.000 (4.48)
StdUNet	GDL-BCE	×	4.75	0.684 (5.02)	4.569 (5.18)	2 (4.49)	0.667 (4.35)	6.722 (4.70)
ResUNet	GDL-BCE	×	4.83	0.674 (5.39)	4.274 (4.70)	2 (4.38)	0.636 (5.00)	6.158 (4.67)

Mean rank, defined as the mean case-level rank, is used to order the models. Metrics are reported as medians, with the corresponding mean ranks in parentheses.

**Table C.1: Case-level ranking on the validation set of Mean Teacher versions of the best base model using varying consistency weights.**

consistency weight	mean rank	DSC	AVD	ALD	F1	HD95
5	2.70	0.720 (2.46)	4.177 (2.74)	1 (2.79)	0.667 (2.94)	5.104 (2.55)
1	2.78	0.720 (2.66)	3.549 (2.80)	2 (2.94)	0.667 (2.74)	5.325 (2.75)
$\times^a$	2.78	0.712 (2.70)	3.481 (2.68)	1 (2.83)	0.667 (2.80)	5.408 (2.90)
50	3.20	0.661 (3.54)	4.845 (3.11)	2 (2.98)	0.667 (3.00)	7.614 (3.35)
20	3.55	0.673 (3.64)	5.691 (3.67)	3 (3.46)	0.571 (3.52)	6.917 (3.44)

Mean rank, defined as the mean case-level rank, is used to order the models. Metrics are reported as medians, with the corresponding mean ranks in parentheses.

<sup>a</sup>The model corresponds to the variant without MT (ISLA-B).



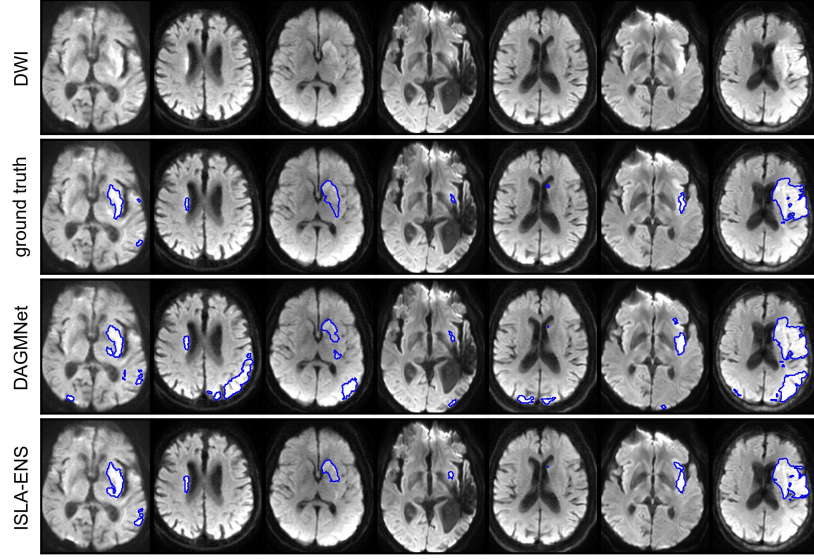


**Figure D.1: Cases from the test set with DAGMNet false positives in the posterior region of the brain.** Each column represents a different participant. The trace diffusion-weighted image and the segmentation masks were registered in a common space (Section 3.2.1).

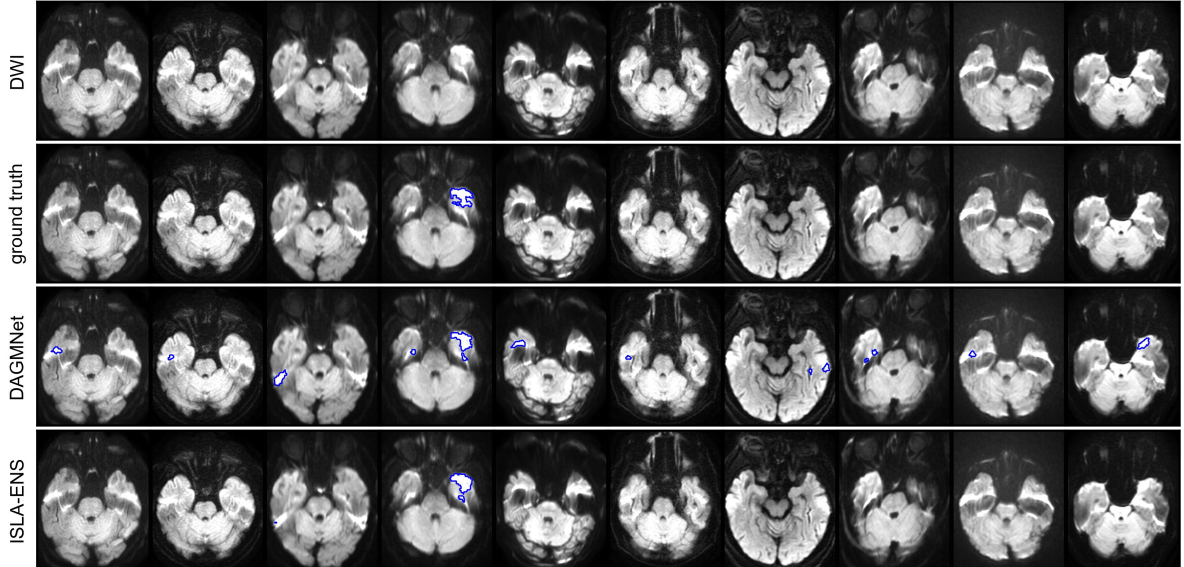


**Figure D.2: Cases from the test set with DAGMNet false positives in the anterior inferior region of the brain.** Each column represents a different participant. The trace diffusion-weighted image and the segmentation masks were registered in a common space (Section 3.2.1).

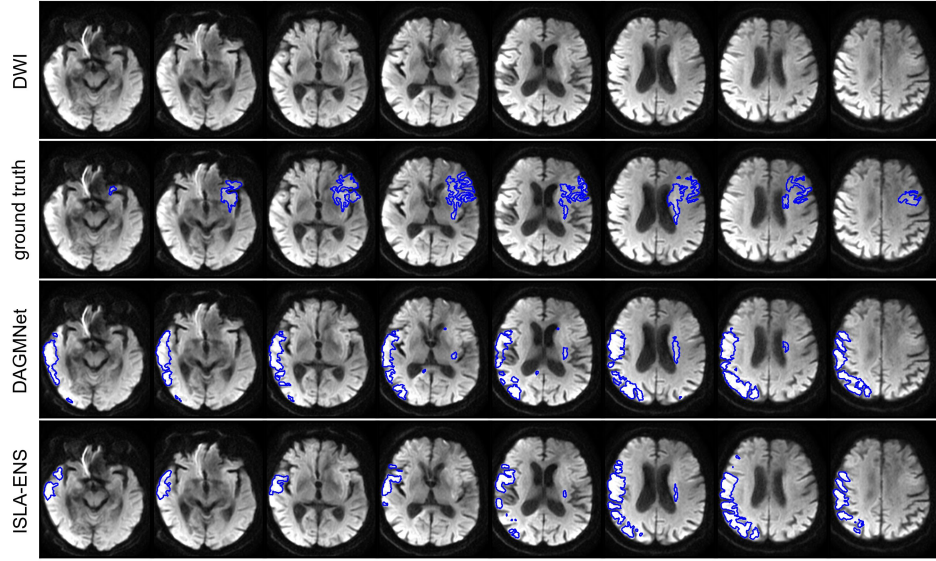


**Figure D.3:** Case from the test set with a false positive lesion produced by DAGMNet and ISLA-ENS due to an inhomogeneity artifact. The trace diffusion-weighted image and the segmentation masks were registered in a common space (Section 3.2.1).

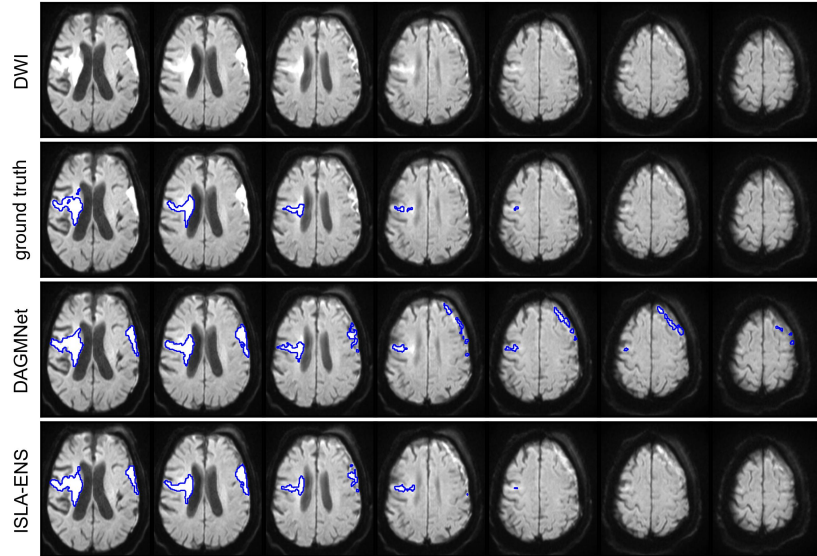


**Figure D.4:** Case from the test set with a false positive lesion produced by DAGMNet and ISLA-ENS due to a hematoma. The trace diffusion-weighted image and the segmentation masks were registered in a common space (Section 3.2.1).

## Appendix E. Exemple of attention coefficients from Attention Gate module

Figure E.1 shows the attention coefficients extracted from ISLA-B during inference on a test-set case. Specifically, the coefficients were taken from the AGs modules of ISLA-B and were upsampled using trilinear interpolation to match the original image resolution.

## Appendix F. Additional metrics on the test set

Table F.1 reports the median and interquartile range for DSC, precision, and recall across the test set.

## Appendix G. Comparison of DeepISLES and ISLA-ENS segmentations on a test-set case

Figure G.1 shows a representative example from the test set with DeepISLES and ISLA-ENS segmentations.

## Appendix H. Case-level ranking of DeepISLES and its constituent models

Table H.1 shows the case-level ranking of DeepISLES and its three constituent models—since DeepISLES is an ensemble approach—on the test set.

## References

Abbasi, H., Orouskhani, M., Asgari, S., Zadeh, S.S., 2023. Automatic brain ischemic stroke segmentation with deep learning: A review. *Neuroscience Informatics* 3, 100145. doi:10.1016/j.neuri.2023.100145.

Abbasi, S., Lan, H., Choupan, J., Sheikh-Bahaei, N., Pandey, G., Varghese, B., 2024. Deep learning for the harmonization of structural mri scans: a survey. *BioMedical Engineering OnLine* 23. doi:10.1186/s12938-024-01280-6.

Abramova, V., Clérigues, A., Quiles, A., Figueredo, D.G., Silva, Y., Pedraza, S., Oliver, A., Lladó, X., 2021. Hemorrhagic stroke lesion segmentation using a 3d u-net with squeeze-and-excitation blocks. *Computerized Medical Imaging and Graphics* 90, 101908. doi:10.1016/j.compmedimag.2021.101908.

Absher, J., Goncher, S., Newman-Norlund, R., Perkins, N., Yourganov, G., Vargas, J., Sivakumar, S., Parti, N., Sternberg, S., Teghipco, A., Gibson, M., Wilson, S., Bonilha, L., Rorden, C., 2024. The stroke outcome optimization project: Acute ischemic strokes from a comprehensive stroke center. *Scientific Data* 11. doi:10.1038/s41597-024-03667-5.

Alis, D., Yergin, M., Alis, C., Topel, C., Asmakutlu, O., Bagcilar, O., Senli, Y.D., Ustundag, A., Salt, V., Dogan, S.N., Velioglu, M., Selcuk, H.H., Kara, B., Okuz, I., Kizilkilic, O., Karaarslan, E., 2021. Inter-vendor performance of deep learning in segmenting acute ischemic lesions on diffusion-weighted imaging: a multicenter study. *Scientific Reports* 11. doi:10.1038/s41598-021-91467-x.

Alshehri, F., Muhammad, G., 2023. A few-shot learning-based ischemic stroke segmentation system using weighted mri fusion. *Image and Vision Computing* 140, 104865. doi:10.1016/j.imavis.2023.104865.

Baaklini, M., Valdés Hernández, M.d.C., 2025. Deep learning for mri-based acute and subacute ischaemic stroke lesion segmentation—a systematic review, meta-analysis, and pilot evaluation of key results. *Frontiers in Medical Technology* 7. doi:10.3389/fmedt.2025.1491197.

Bojsen, J.A., Elhakim, M.T., Graumann, O., Gaist, D., Nielsen, M., Harbo, F.S.G., Krag, C.H., Sagar, M.V., Kruuse, C., Boesen, M.P., Rasmussen, B.S.B., 2024. Artificial intelligence for mri stroke detection: a systematic review and meta-analysis. *Insights into Imaging* 15. doi:10.1186/s13244-024-01723-7.

Bridge, C.P., Bizzo, B.C., Hillis, J.M., Chin, J.K., Comeau, D.S., Gauriau, R., Macruz, F., Pawar, J., Noro, F.T.C., Sharaf, E., Straus Takahashi, M., Wright, B., Kalafut, J.F., Andriole, K.P., Pomerantz, S.R., Pedemonte, S., González, R.G., 2022. Development and clinical application of a deep learning model to identify acute infarct on magnetic resonance imaging. *Scientific Reports* 12. doi:10.1038/s41598-022-06021-0.

Capirossi, C., Laiso, A., Renieri, L., Capasso, F., Limbucci, N., 2023. Epidemiology, organization, diagnosis and treatment of acute ischemic stroke. *European Journal of Radiology Open* 11, 100527. doi:10.1016/j.ejro.2023.100527.

Cimflova, P., Kral, J., Volny, O., Horn, M., Ojha, P., Cabal, M., Kasickova, L., Havelka, J., Jonszta, T., Bar, M., Qiu, W., 2021. Mri diffusion-weighted imaging to measure infarct volume: Assessment of manual segmentation variability. *Journal of Neuroimaging* 31, 541–550. doi:10.1111/jon.12850.

Clérigues, A., Valverde, S., Bernal, J., Freixenet, J., Oliver, A., Lladó, X., 2019. Acute ischemic stroke lesion core segmentation in ct perfusion images using fully convolutional neural networks. *Computers in Biology and Medicine* 115, 103487. doi:10.1016/j.combiomed.2019.103487.

Clérigues, A., Valverde, S., Bernal, J., Freixenet, J., Oliver, A., Lladó, X., 2020. Acute and sub-acute stroke lesion segmentation from multimodal mri. *Computer*

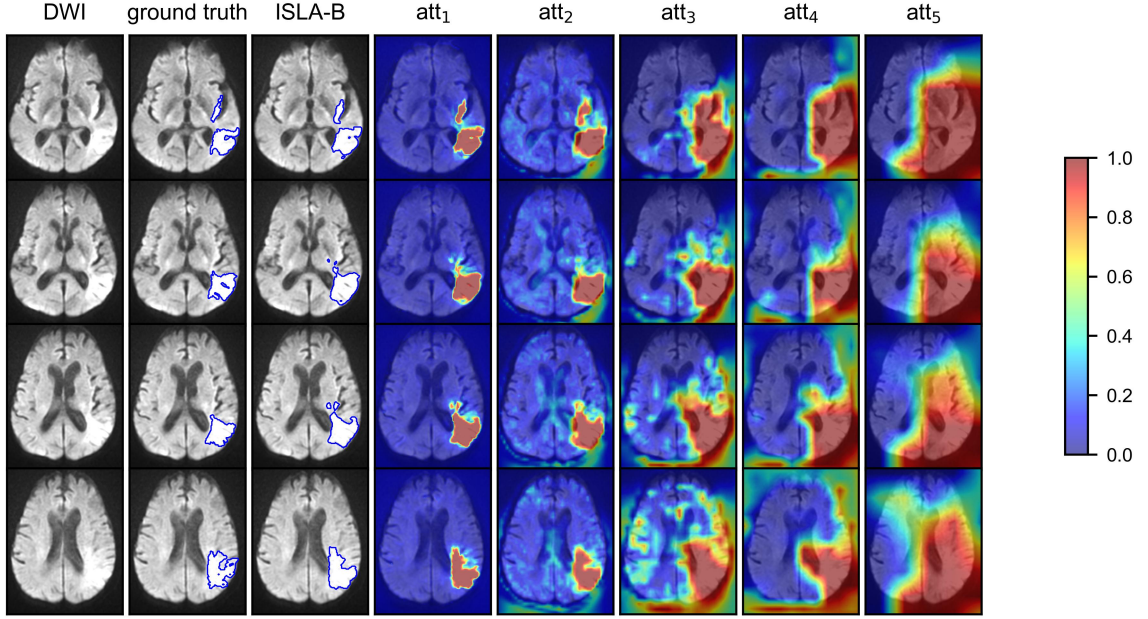


**Figure E.1: Illustration of attention coefficients computed by ISLA-B during inference on a test-set case.** The coefficients were extracted from the AGs modules.  $\text{att}_i$  denotes the coefficients at the  $i$ -th U-Net level (from higher to lower resolution). Trilinear upsampling was applied to make attention maps match the original image resolution (not for  $\text{att}_1$ ).

**Table F.1: Dice similarity coefficient, precision and recall in the test set.**

	DeepISLES	DAGMNet	ISLA-B	ISLA-MT	ISLA-ENS
<b>DSC</b>	0.512 (0.716)	0.724 (0.259)	0.741 (0.187)	0.734 (0.201)	0.754 (0.167)
<b>precision</b>	0.930 (0.185)	0.757 (0.302)	0.766 (0.221)	0.776 (0.228)	0.773 (0.204)
<b>recall</b>	0.368 (0.705)	0.785 (0.259)	0.748 (0.234)	0.762 (0.233)	0.764 (0.225)

Values are expressed as median (interquartile range).

**Table H.1: Case-level ranking of DeepISLES and its constituent models on the test set.**

model	mean rank	DSC	AVD	ALD	F1	HD95
DeepISLES	2.22	0.512 (2.17)	5.933 (2.22)	2 (2.30)	0.667 (2.19)	18.529 (2.25)
NVAUTO	2.47	0.657 (2.09)	10.494 (2.47)	3 (2.93)	0.500 (2.67)	13.936 (2.17)
SWAN	2.49	0.460 (2.68)	5.953 (2.48)	1 (2.31)	0.615 (2.41)	20.547 (2.57)
SEALS	2.82	0.080 (3.06)	9.898 (2.83)	2 (2.47)	0.500 (2.73)	42.443 (3.01)

Mean rank, defined as the mean case-level rank, is used to order the models. Metrics are reported as medians, with the corresponding mean ranks in parentheses.



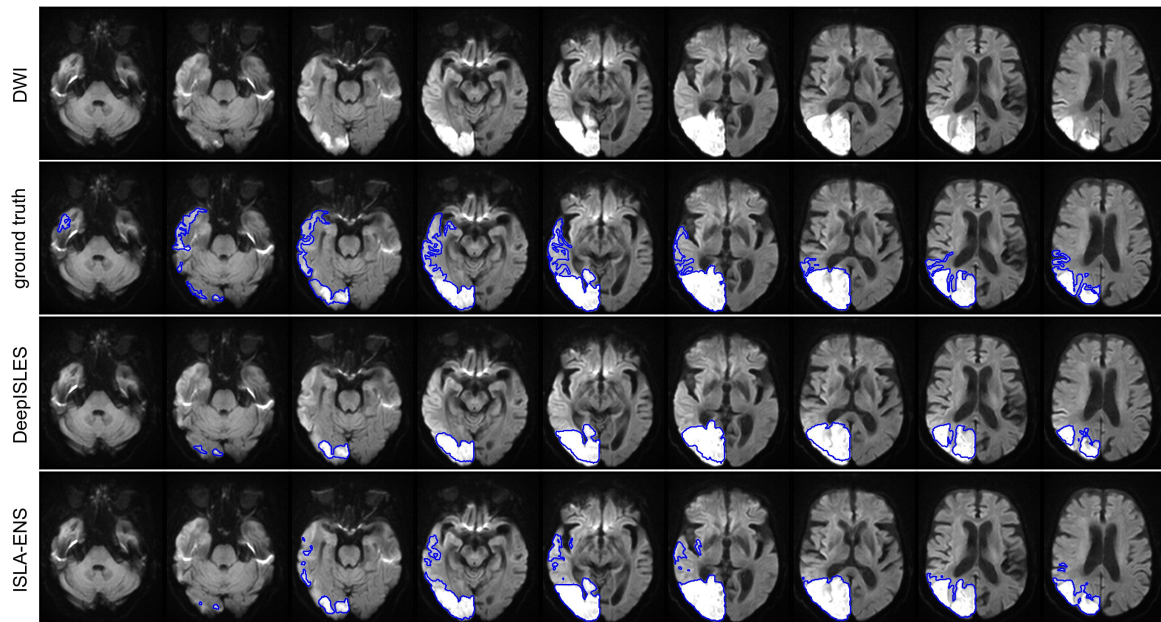


**Figure G.1: An illustrative case of DeepISLES and ISLA-ENS segmentations from the test set.** Axial slices are shown from the volume corresponding to the median difference in DSC between the two models across the test set. The trace diffusion-weighted image and the segmentation masks were registered in a common space (Section 3.2.1).

- Methods and Programs in Biomedicine 194, 105521. doi:10.1016/j.cmpb.2020.105521.
- Dinsdale, N.K., Jenkinson, M., Namburete, A.I., 2021. Deep learning-based unlearning of dataset bias for mri harmonisation and confound removal. *NeuroImage* 228, 117689. doi:10.1016/j.neuroimage.2020.117689.
- French, G., Mackiewicz, M., Fisher, M., 2017. Self-ensembling for visual domain adaptation. doi:10.48550/ARXIV.1706.05208.
- Gheibi, Y., Shirini, K., Razavi, S.N., Farhoudi, M., Samad-Soltani, T., 2023. Cnn-res: deep learning framework for segmentation of acute ischemic stroke lesions on multimodal mri images. *BMC Medical Informatics and Decision Making* 23. doi:10.1186/s12911-023-02289-y.
- Gómez, S., Mantilla, D., Rangel, E., Ortiz, A., D Vera, D., Martínez, F., 2023. A deep supervised cross-attention strategy for ischemic stroke segmentation in mri studies. *Biomedical Physics & Engineering Express* 9, 035026. doi:10.1088/2057-1976/acc853.
- Hatamizadeh, A., Tang, Y., Nath, V., Yang, D., Myronenko, A., Landman, B., Roth, H.R., Xu, D., 2022. Unetr: Transformers for 3d medical image segmentation, in: *Proceedings of the IEEE/CVF Winter Conference on Applications of Computer Vision (WACV)*, pp. 574–584.
- He, K., Zhang, X., Ren, S., Sun, J., 2016. Deep residual learning for image recognition, in: *Proceedings of the IEEE Conference on Computer Vision and Pattern Recognition (CVPR)*.
- Hernandez Petzsche, M.R., de la Rosa, E., Hanning, U., Wiest, R., Valenzuela, W., Reyes, M., Meyer, M., Liew, S.L., Kofler, F., Ezhov, I., Robben, D., Hutton, A., Friedrich, T., Zarth, T., Bürkle, J., Baran, T.A., Menze, B., Broocks, G., Meyer, L., Zimmer, C., Boeckh-Behrens, T., Berndt, M., Ikenberg, B., Wiestler, B., Kirschke, J.S., 2022. Isles 2022: A multi-center magnetic resonance imaging stroke lesion segmentation dataset. *Scientific Data* 9. doi:10.1038/s41597-022-01875-5.
- Hoopes, A., Mora, J.S., Dalca, A.V., Fischl, B., Hoffmann, M., 2022. Synthstrip: skull-stripping for any brain image. *NeuroImage* 260, 119474. doi:10.1016/j.neuroimage.2022.119474.
- Hu, J., Shen, L., Albanie, S., Sun, G., Wu, E., 2020. Squeeze-and-excitation networks. *IEEE Transactions on Pattern Analysis and Machine Intelligence* 42, 2011–2023. doi:10.1109/tpami.2019.2913372.
- Jenkinson, M., Bannister, P., Brady, M., Smith, S., 2002. Improved optimization for the robust and accurate linear registration and motion correction of brain images. *NeuroImage* 17, 825–841. doi:10.1006/nimg.2002.1132.
- Kingma, D.P., Ba, J., 2014. Adam: A method for stochastic optimization. doi:10.48550/ARXIV.1412.6980.
- Lee, C.Y., Xie, S., Gallagher, P., Zhang, Z., Tu, Z., 2015. Deeply-Supervised Nets, in: *Lebanon, G., Vish-*

- wanathan, S.V.N. (Eds.), Proceedings of the Eighteenth International Conference on Artificial Intelligence and Statistics, PMLR, San Diego, California, USA. pp. 562–570. URL: <https://proceedings.mlr.press/v38/lee15a.html>.
- Li, T., An, X., Di, Y., Gui, C., Yan, Y., Liu, S., Ming, D., 2024. Srsnet: Accurate segmentation of stroke lesions by a two-stage segmentation framework with asymmetry information. *Expert Systems with Applications* 254, 124329. doi:10.1016/j.eswa.2024.124329.
- Li, X., Zhao, Y., Jiang, J., Cheng, J., Zhu, W., Wu, Z., Jing, J., Zhang, Z., Wen, W., Sachdev, P.S., Wang, Y., Liu, T., Li, Z., 2022. White matter hyperintensities segmentation using an ensemble of neural networks. *Human Brain Mapping* 43, 929–939. doi:10.1002/hbm.25695.
- Li, Y., Wang, N., Shi, J., Hou, X., Liu, J., 2018. Adaptive batch normalization for practical domain adaptation. *Pattern Recognition* 80, 109–117. doi:10.1016/j.patcog.2018.03.005.
- Lin, T.Y., Goyal, P., Girshick, R., He, K., Dollar, P., 2020. Focal loss for dense object detection. *IEEE Transactions on Pattern Analysis and Machine Intelligence* 42, 318–327. doi:10.1109/tpami.2018.2858826.
- Liu, C.F., Hsu, J., Xu, X., Ramachandran, S., Wang, V., Miller, M.I., Hillis, A.E., Faria, A.V., Wintermark, M., Warach, S.J., Albers, G.W., Davis, S.M., Grotta, J.C., Hacke, W., Kang, D.W., Kidwell, C., Koroshetz, W.J., Lees, K.R., Lev, M.H., Liebeskind, D.S., Sorensen, A.G., Thijs, V.N., Thomalla, G., Wardlaw, J.M., Luby, M., 2021. Deep learning-based detection and segmentation of diffusion abnormalities in acute ischemic stroke. *Communications Medicine* 1. doi:10.1038/s43856-021-00062-8.
- Liu, L., Kurgan, L., Wu, F.X., Wang, J., 2020. Attention convolutional neural network for accurate segmentation and quantification of lesions in ischemic stroke disease. *Medical Image Analysis* 65, 101791. doi:10.1016/j.media.2020.101791.
- Luo, J., Dai, P., He, Z., Huang, Z., Liao, S., Liu, K., 2024. Deep learning models for ischemic stroke lesion segmentation in medical images: A survey. *Computers in Biology and Medicine* 175, 108509. doi:10.1016/j.combiomed.2024.108509.
- Lv, P., Wang, J., Zhang, X., Shi, C., 2022. Deep supervision and atrous inception-based u-net combining crf for automatic liver segmentation from ct. *Scientific Reports* 12. doi:10.1038/s41598-022-21562-0.
- Maqsood, R., Abid, F., Rasheed, J., Osman, O., Alsubai, S., 2025. Optimal res-unet architecture with deep supervision for tumor segmentation. *Frontiers in Medicine* 12. doi:10.3389/fmed.2025.1593016.
- Micikevicius, P., Narang, S., Alben, J., Diamos, G., Elsen, E., Garcia, D., Ginsburg, B., Houston, M., Kuchaiev, O., Venkatesh, G., Wu, H., 2017. Mixed precision training. doi:10.48550/ARXIV.1710.03740.
- Moon, H.S., Heffron, L., Mahzarnia, A., Obeng-Gyasi, B., Holbrook, M., Badea, C.T., Feng, W., Badea, A., 2022. Automated multimodal segmentation of acute ischemic stroke lesions on clinical mr images. *Magnetic Resonance Imaging* 92, 45–57. doi:10.1016/j.mri.2022.06.001.
- Nazari-Farsani, S., Yu, Y., Duarte Armindo, R., Lansberg, M., Liebeskind, D.S., Albers, G., Christensen, S., Levin, C.S., Zaharchuk, G., 2023. Predicting final ischemic stroke lesions from initial diffusion-weighted images using a deep neural network. *NeuroImage: Clinical* 37, 103278. doi:10.1016/j.nicl.2022.103278.
- Perone, C.S., Ballester, P., Barros, R.C., Cohen-Adad, J., 2019. Unsupervised domain adaptation for medical imaging segmentation with self-ensembling. *NeuroImage* 194, 1–11. doi:10.1016/j.neuroimage.2019.03.026.
- Platscher, M., Zopes, J., Federau, C., 2022. Image translation for medical image generation: Ischemic stroke lesion segmentation. *Biomedical Signal Processing and Control* 72, 103283. doi:10.1016/j.bspc.2021.103283.
- Plis, S.M., Masoud, M., Hu, F., Hanayik, T., Ghosh, S.S., Drake, C., Newman-Norlund, R., Rorden, C., 2024. Brainchop: Providing an edge ecosystem for deployment of neuroimaging artificial intelligence models. *Aperture Neuro* 4. doi:10.52294/001c.123059.
- Rahman, A., Chowdhury, M.E., Ibne Wadud, M.S., Sarmun, R., Mushtak, A., Zoghoul, S.B., Al-Hashimi, I., 2025. Deep learning-driven segmentation of ischemic stroke lesions using multi-channel mri. *Biomedical Signal Processing and Control* 105, 107676. doi:10.1016/j.bspc.2025.107676.
- Roca, V., Kuchcinski, G., Pruvo, J.P., Manouvriez, D., Lopes, R., 2025. IGUANe: A 3D generalizable CycleGAN for multicenter harmonization of brain MR images. *Medical Image Analysis* 99, 103388. doi:10.1016/j.media.2024.103388.
- de la Rosa, E., Reyes, M., Liew, S.L., Hutton, A., Wiest, R., Kaesmacher, J., Hanning, U., Hakim, A., Zubal, R., Valenzuela, W., Robben, D., Sima, D.M., Anania, V., Brys, A., Meakin, J.A., Mickan, A., Broocks, G., Heitkamp, C., Gao, S., Liang, K., Zhang, Z., Rahman Siddiquee, M.M., Myronenko, A., Ashtari, P., Van Huffel, S., Jeong, H., Yoon, C., Kim, C., Huo, J., Ourselin, S., Sparks, R., Clèrigues, A., Oliver, A., Lladó, X., Chalcraft, L., Pappas, I., Bertels, J., Heylen, E., Moreau, J., Hatami, N., Frindel, C., Qayyum, A., Mazher, M., Puig, D., Lin, S.C., Juan, C.J., Hu, T., Boone, L., Goubran, M., Liu, Y.J., Wegener,

- S., Kofler, F., Ezhov, I., Shit, S., Hernandez Petzsche, M.R., Müller, M., Menze, B., Kirschke, J.S., Wiestler, B., 2025. Deepisles: a clinically validated ischemic stroke segmentation model from the isles'22 challenge. *Nature Communications* 16. doi:10.1038/s41467-025-62373-x.
- Rundo, L., Han, C., Nagano, Y., Zhang, J., Hataya, R., Militello, C., Tangherloni, A., Nobile, M.S., Ferretti, C., Besozzi, D., Gilardi, M.C., Vitabile, S., Mauri, G., Nakayama, H., Cazzaniga, P., 2019. Use-net: Incorporating squeeze-and-excitation blocks into u-net for prostate zonal segmentation of multi-institutional mri datasets. *Neurocomputing* 365, 31–43. doi:10.1016/j.neucom.2019.07.006.
- Ryu, W.S., Schellingerhout, D., Park, J., Chung, J., Jeong, S.W., Gwak, D.S., Kim, B.J., Kim, J.T., Hong, K.S., Lee, K.B., Park, T.H., Park, S.S., Park, J.M., Kang, K., Cho, Y.J., Park, H.K., Lee, B.C., Yu, K.H., Oh, M.S., Lee, S.J., Kim, J.G., Cha, J.K., Kim, D.H., Lee, J., Park, M.S., Kim, D., Bang, O.Y., Kim, E.Y., Sohn, C.H., Kim, H., Bae, H.J., Kim, D.E., 2025. Deep learning-based automatic segmentation of cerebral infarcts on diffusion mri. *Scientific Reports* 15. doi:10.1038/s41598-025-91032-w.
- Schlemper, J., Oktay, O., Schaap, M., Heinrich, M., Kainz, B., Glocker, B., Rueckert, D., 2019. Attention gated networks: Learning to leverage salient regions in medical images. *Medical Image Analysis* 53, 197–207. doi:10.1016/j.media.2019.01.012.
- Sheng, M., Xu, W., Yang, J., Chen, Z., 2022. Cross-attention and deep supervision unet for lesion segmentation of chronic stroke. *Frontiers in Neuroscience* 16. doi:10.3389/fnins.2022.836412.
- Sudre, C.H., Li, W., Vercauteren, T., Ourselin, S., Jorge Cardoso, M., 2017. Generalised Dice Overlap as a Deep Learning Loss Function for Highly Unbalanced Segmentations. Springer International Publishing. p. 240–248. doi:10.1007/978-3-319-67558-9\_28.
- Tarvainen, A., Valpola, H., 2017. Mean teachers are better role models: Weight-averaged consistency targets improve semi-supervised deep learning results. *Advances in neural information processing systems* 30.
- Trebing, K., Stańczyk, T., Mehrkanon, S., 2021. Smaat-unet: Precipitation nowcasting using a small attention-unet architecture. *Pattern Recognition Letters* 145, 178–186. doi:10.1016/j.patrec.2021.01.036.
- Wang, R., Chaudhari, P., Davatzikos, C., 2022. Embracing the disharmony in medical imaging: A simple and effective framework for domain adaptation. *Medical Image Analysis* 76, 102309. doi:10.1016/j.media.2021.102309.
- Wang, Z., Zhu, H., Huang, B., Wang, Z., Lu, W., Chen, N., Wang, Y., 2023. M-msseu: source-free domain adaptation for multi-modal stroke lesion segmentation using shadowed sets and evidential uncertainty. *Health Information Science and Systems* 11. doi:10.1007/s13755-023-00247-6.
- Wiltgen, T., McGinnis, J., Schlaeger, S., Kofler, F., Voon, C., Berthele, A., Bischl, D., Grundl, L., Will, N., Metz, M., Schinz, D., Sepp, D., Prucker, P., Schmitz-Koep, B., Zimmer, C., Menze, B., Rueckert, D., Hemmer, B., Kirschke, J., Mühlau, M., Wiestler, B., 2024. Lst-ai: A deep learning ensemble for accurate ms lesion segmentation. *NeuroImage: Clinical* 42, 103611. doi:10.1016/j.nicl.2024.103611.
- Woo, S., Park, J., Lee, J.Y., Kweon, I.S., 2018. CBAM: Convolutional Block Attention Module. Springer International Publishing. p. 3–19. doi:10.1007/978-3-030-01234-2\_1.
- Wu, Y., He, K., 2018. Group Normalization. Springer International Publishing. p. 3–19. doi:10.1007/978-3-030-01261-8\_1.
- Yeung, M., Sala, E., Schönlieb, C.B., Rundo, L., 2022. Unified focal loss: Generalising dice and cross entropy-based losses to handle class imbalanced medical image segmentation. *Computerized Medical Imaging and Graphics* 95, 102026. doi:10.1016/j.compmedimag.2021.102026.
- Yu, W., Huang, Z., Zhang, J., Shan, H., 2023. San-net: Learning generalization to unseen sites for stroke lesion segmentation with self-adaptive normalization. *Computers in Biology and Medicine* 156, 106717. doi:10.1016/j.compbimed.2023.106717.
- Yu, Y., Xie, Y., Thamm, T., Gong, E., Ouyang, J., Christensen, S., Marks, M., Lansberg, M., Albers, G., Zaharchuk, G., 2021. Tissue at risk and ischemic core estimation using deep learning in acute stroke. *American Journal of Neuroradiology* 42, 1030–1037. doi:10.3174/ajnr.a7081.
- Yu, Y., Xie, Y., Thamm, T., Gong, E., Ouyang, J., Huang, C., Christensen, S., Marks, M.P., Lansberg, M.G., Albers, G.W., Zaharchuk, G., 2020. Use of deep learning to predict final ischemic stroke lesions from initial magnetic resonance imaging. *JAMA Network Open* 3, e200772. doi:10.1001/jamanetworkopen.2020.0772.
- Zafari-Ghadim, Y., Rashed, E.A., Mohamed, A., Mabrok, M., 2024. Transformers-based architectures for stroke segmentation: a review. *Artificial Intelligence Review* 57. doi:10.1007/s10462-024-10900-5.
- Zhang, Z., Liu, Q., Wang, Y., 2018. Road extraction by deep residual u-net. *IEEE Geoscience and Remote Sensing Letters* 15, 749–753. doi:10.1109/lgrs.2018.2802944.